



34 importance of incorporating fog deposition as an additional scavenging mechanism in dispersion
35 modeling under foggy conditions.

36

37 **Keywords:** Radiation fog, fog microphysics, desert regions, fog deposition velocity, fog water
38 deposition flux, fog monitor, Weather Research Forecasting (WRF) model.

39 1. Introduction

40

41 Following the Fukushima accident and its consequences in Japan, it was recognized that cloud and
42 fog waters may have contributed to the radioactive contamination of soil and forest ecosystems
43 (Imamura et al., 2020). This was experimentally demonstrated thanks to field observations at
44 elevated sites that experienced cloudy conditions in Japan during the nuclear accident (Hososhima
45 and Kaneyasu, 2015; Kaneyasu et al., 2022).

46

47 Subject to the capabilities of trace level measurement, Masson et al. (2015) found that the detection
48 of ^{134}Cs (a radionuclide released during the accident with a half-life of 2.06 year) was possible
49 over a longer time scale in cloud water, compared to its detection in aerosols and rainwater. Wet
50 deposition by fog has triggered attention for their chemical content (e.g., NH_4^+ , SO_2^-), and more
51 generally as regards the issue of acidified precipitations and forest decline (Hůnová et al., 2011;
52 Katata, 2014), as well as for their organic content (Eckardt and Schemenauer, 1998; Kaseke et al.,
53 2018). In light of the various and sometimes severe impacts of fog on the environment, human
54 activities (e.g., airport traffic disruption) and human health, fog research and studies have a long
55 rich history (Pérez-Díaz et al., 2017). While there has been growing interest in the study of fog in
56 arid and semi-arid regions (Eckardt and Schemenauer, 1998; Feigenwinter et al., 2020; Katata et
57 al., 2010; Spirig et al., 2021), research on fog deposition and impact on radionuclides settlement
58 in such environments is notably lacking.

59

60 Similarly to cloud water, fog water is also prone to be enriched in atmospheric chemicals or
61 radioactive compounds. Deposition velocity of fog water droplets depends on both the droplet size
62 (up to several tens μm) and turbulent movements induced by obstacles (canopy, plant density,
63 roughness scale, foliar index) and wind components (Tav et al., 2018). Tav et al. (2018) showed
64 that the fog droplet deposition velocity was similar to the gravitational settling velocity on bare
65 soils but was systematically higher above short plants and grass. Additionally, rainwater
66 monitoring networks (i.e., rain gauges) and rain radars are not sensitive enough to quantify the
67 amount of fogwater deposited. As a result, fog deposition is often called “occult deposition”. Once
68 deposited, water will evaporate and the dry solute will stay on the deposition surface. From the
69 modeling point of view, and to a few exceptions (Katata, 2014), radionuclide deposition during
70 fog and cloud events is usually not taken into account in emergency situations response models or
71 even less in routine conditions.



72 Fog is a common occurrence in the United Arab Emirates (UAE), which is situated on the
73 northeastern coast of the Arabian Peninsula. Despite being an arid country with desert as the main
74 land cover type (Fonseca et al., 2023; Francis et al., 2021; Nelli et al., 2022), the majority of low
75 visibility events (< 1 km) during winter in the UAE are due to condensation processes (Aldababseh
76 and Temimi, 2017). Fog occurs mostly in winter, with up to 13 fog days per month and 51 fog
77 days per year reported at the international airport in Abu Dhabi (Mohan et al., 2020); (Weston and
78 Temimi, 2020; Weston et al., 2021a). The most common fog type is radiation fog, which depends
79 on the land-sea breeze for its formation (Fonseca et al., 2023; Mohan et al., 2020; Weston and
80 Temimi, 2020; Weston et al., 2021a). Most events last 1 hour or less, but events longer than 9
81 hours have been observed in January and December (Fonseca et al., 2023; Mohan et al., 2020;
82 Weston and Temimi, 2020; Weston et al., 2021a). Fonseca et al. (2023) examined the atmospheric
83 circulation patterns that favor the occurrence of long-lasting fog events in the UAE, and found a
84 positive trend in the frequency of such occurrences in recent decades.

85 Although previous analyses of fog in the UAE have been conducted using satellite data (Weston
86 and Temimi, 2020a) and in-situ measurements for a single fog event (Weston et al., 2022), a
87 comprehensive observational analysis of fog microphysics and dynamics in the region has not yet
88 been carried out. This paper addresses this gap by examining the dynamics and microphysics of
89 12 fog events during the 2021-2022 winter season to determine fog deposition velocity, a crucial
90 parameter for atmospheric dispersion and deposition applications.

91 Fog deposition velocity plays a significant role in estimating pollutant and radionuclide deposition
92 rates in the environment. However, this parameter has not been estimated for the UAE, despite the
93 country experiencing an average of 50 days of radiation fog per year. Besides allowing for an
94 improvement of the understanding of fog dynamics, an estimation of the fog deposition velocity
95 is crucial for specific applications such as dispersion and deposition models and air quality.
96 Regarding the former, and as noted by Imamura et al. (2020), the ground deposition of radioactive
97 material may be increased in the presence of fog owing to the potential entrainment of the
98 radionuclides into the water droplets and their subsequent gravitational sedimentation to the
99 surface. Incorporating deposition velocity in foggy conditions can therefore improve the accuracy
100 and representativeness of radionuclide dispersion and deposition.

101 The objectives of this study are as follows: (1) Present the first observation-derived fog
102 deposition velocity for the UAE, (2) Assess, through numerical modeling, the impact of fog on
103 radionuclides dispersion for a given case study. The paper is organized as follows: in section 2,
104 the data and methods used in this study are described. In section 3, we analyze the fog microphysics
105 and dynamics. Section 4 details the fog deposition velocity analysis. Section 5 addresses the impact
106 of fog on the dispersion and deposition of radionuclides in the UAE for a given case study.
107 Conclusions are drawn in section 6.



108 2. Data and Methods

109 2.1 Site Description

110 The Barakah Nuclear Power Plant (BNPP) is situated in a low-lying coastal region in the UAE's
111 hyperarid western region. According to Nesterov et al. (2021), the site experiences a seasonal mean
112 local sea surface temperature (SST) ranging from about 21°C in winter to 33°C in summer, which
113 is slightly lower than SSTs further east around Abu Dhabi and Dubai. This creates a steeper land-
114 sea temperature gradient, resulting in stronger sea-breeze circulations at the site. Nelli et al. (2022)
115 reported that the wind speeds at the site of interest are generally below 5 ms⁻¹, blowing mainly
116 from a northerly direction. The wind intensifies at around 12–18 Local Time (LT) and 02–09 LT
117 due to the sea-breeze and the downward mixing of momentum from the nighttime low-level jet,
118 respectively. Winter sees stronger winds, which vary mostly in response to mid-latitude baroclinic
119 systems, while summer experiences more quiescent conditions due to the site's proximity to the
120 core of the Arabian Heat Low (AHL) (Fonseca et al., 2022). The colder nights and weaker wind
121 speeds from December to February are favorable for radiation fog occurrence, with peak fog
122 formation around local sunrise. Organized convective systems lead to deep and very deep
123 convective clouds in March–April, with generally reduced cloud cover from May to October (Nelli
124 et al., 2021b). The region of interest experiences a monthly-mean aerosol optical depth ranging
125 from ~0.3 in December–January to ~1.2 in July due to increased exposure to dust storms in the
126 summer season. Dust activity peaks during winter and spring associated with the intrusion of cold
127 fronts from mid-latitudes, as reported by Nelli et al. (2020b, 2022).

128 2.2 Field experiment setup

129 2.2.1 Horizontal Visibility

130 A SENTRY™ Visibility Sensor 1 (SVS1) instrument was used to measure visibility. The
131 instrument estimates the scattering of visible light by the atmosphere to calculate the extinction
132 coefficient, μ , which represents the amount of attenuation of a beam due to scattering and
133 absorption by aerosols. Horizontal visibility data is recorded every minute. Visibility data from
134 SVS1 are validated and extensively used for detecting occurrences of fog and dust at the Abu
135 Dhabi location (Nelli et al., 2022; Temimi et al., 2020a; Weston et al., 2022).

136 2.2.2 Fog Monitor

137 We used a Fog Monitor (FM-120) from Droplet Measurement Technologies to observe and
138 quantify microphysical processes within the fog. This instrument has been largely used in the field
139 and proven to be reliable. Nevertheless, this deployment, to the authors' knowledge, is the first in
140 the region, which allows for comparison with other studies (Gonser et al., 2012; Gultepe et al.,
141 2009, 2021; Mazoyer et al., 2019; Niu et al., 2010). The FM-120 is a forward scattering
142 spectrometer probe that calculates droplet size based on scattered light from a laser and employs



143 Mie theory. The instrument assumes that the droplets are spherical and made of water with a known
144 refractive index. The FM-120 can count droplets diameter in the size range of 2-50 μm , with size
145 bins of 1 μm for droplets $\leq 14 \mu\text{m}$ and size bins of 2 μm for droplets $> 14 \mu\text{m}$ and $\leq 50 \mu\text{m}$. The
146 liquid water content (LWC) is calculated based on the assumption that each droplet is spherical.
147 Data was recorded every second and later aggregated into 1-minute averages. When processing
148 median volume diameter (MVD) data, we only considered values where the number concentration
149 was greater than 2 counts $\text{cm}^{-3} \text{sec}^{-1}$

150 **2.2.3 Microwave Radiometer**

151 We deployed a ground-based passive microwave radiometer (MWR, RPG-HATPRO; G5
152 series) from RPG at the site to measure brightness temperature across 14 channels. The instrument
153 has seven channels in the range 22.24–31.40 GHz (K-Band), which are used for retrieving water
154 vapor, and seven channels between 51.26–58 GHz (V-Band), which are used for retrieving
155 temperature profiles (Rose et al., 2005). The MWR is capable of capturing temperature profiles
156 with a high vertical resolution (30-50 m) in the lower 1,200 m of the atmosphere and humidity
157 profiles with a 100 m resolution in the lower 2,000 m. Here, we analyze the temperature and
158 specific humidity profiles during the fog events. The full description of the operational method
159 and measurement uncertainties are discussed in Temimi et al. (2020a). MWR instrument data over
160 UAE has been extensively used to study the thermodynamic structure of the atmosphere during
161 different weather conditions such as fog, dust storms, cold fronts, and solar eclipses (Nelli et al.,
162 2022, 2021a; Temimi et al., 2020a; Weston et al., 2021b).

163 **2.2.4 Weather Stations**

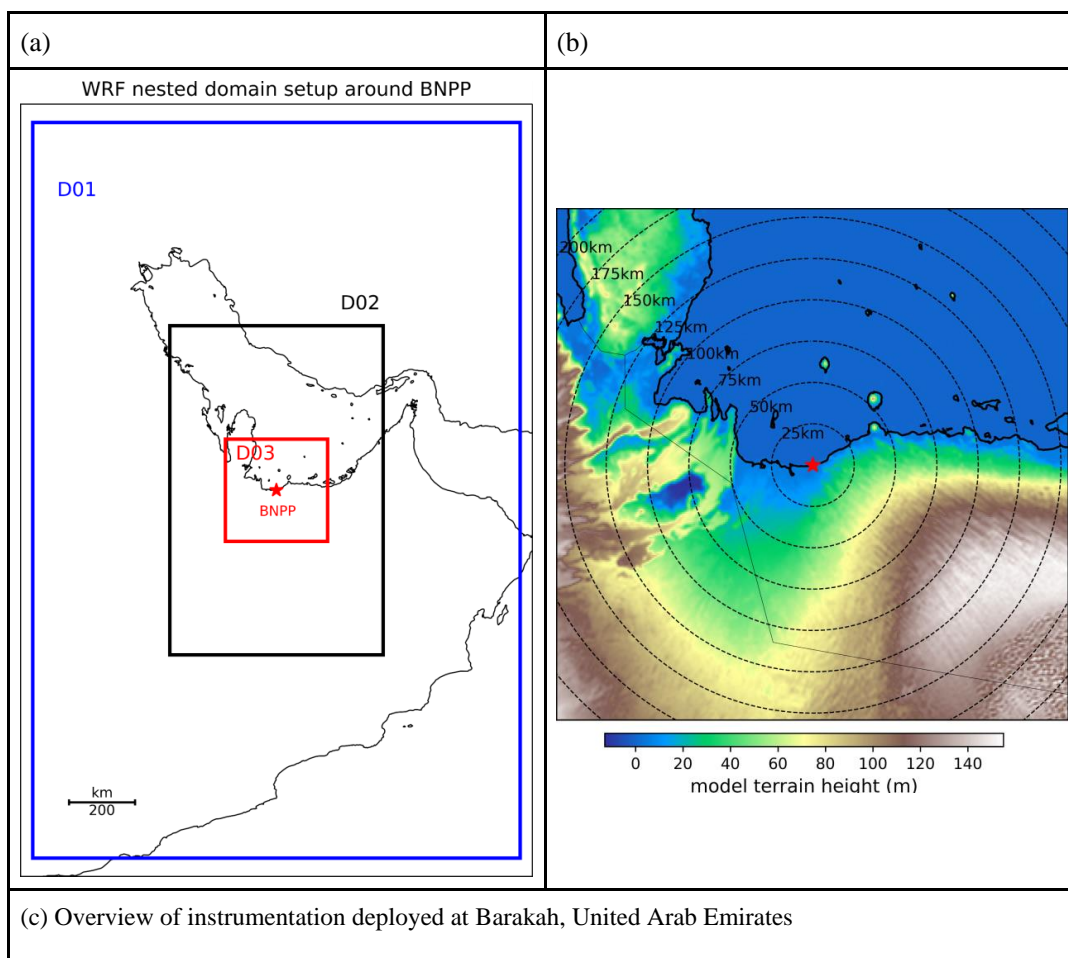
164 A portable weather station equipped with the WS501-UMB smart sensor and SW100 smart
165 disdrometer from LUFT is used to measure meteorological parameters at the site. The parameters
166 measured by this weather station include air temperature, relative humidity, wind speed and
167 direction, global shortwave radiation, precipitation type, and precipitation amount. All parameters
168 are logged at a 1-minute time resolution.

169

170 The experiment site is located within 2 km of the Arabian Gulf in a developing urban
171 region. All the instruments described above, except for the 3D ultrasonic anemometer, were
172 deployed on the rooftop of the Visitor's Badging Office (VBO, 23.968052°N, 52.267309°E),
173 which is roughly 10 m above the ground level. Since this building is far away from major built
174 structures, the measurements are unlikely to be affected by their deployment on its rooftop. The
175 collected measurements and their respective periods are summarized in Table 1. The 3D ultrasonic
176 anemometer is installed at 4-m height on a 10-m high meteorological tower located near the beach
177 area, 23.96333°N, 52.21185°E (Francis et al., 2023; Nelli et al., 2022). The radial distance between
178 the 10-m tower and VBO is approximately 6 km. An overview of the site where the instruments
179 are deployed is given in Nelli et al. (2022). Prior to the present analysis, we applied rigorous quality



180 control procedures described in Rao and Narendra Reddy (2018), Rao and Reddy (2019) to the
181 measurements, which included removing outliers and performing double coordinate rotation on
182 the 3D ultrasonic anemometer data etc.
183



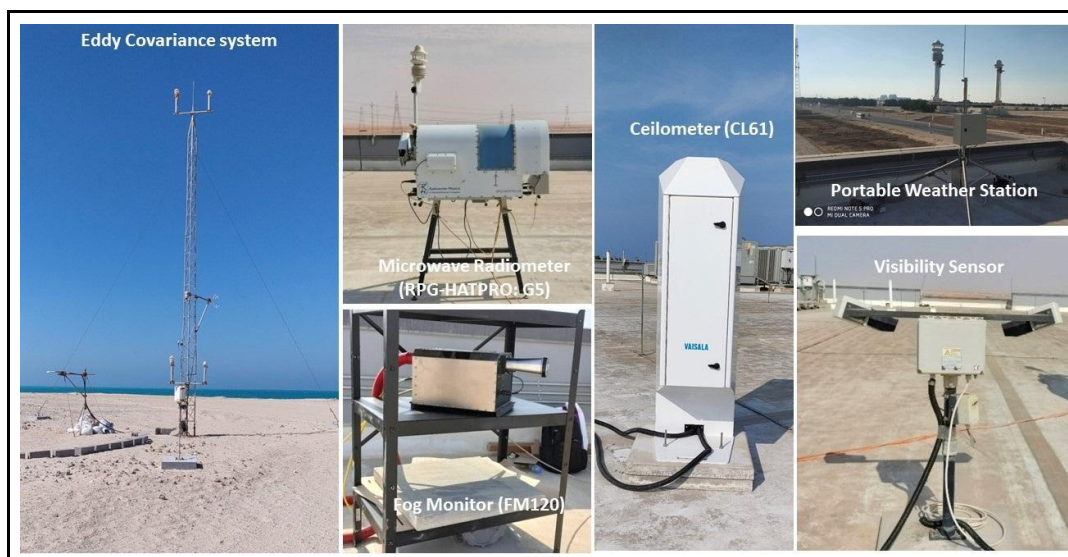


Figure 1: (a) WRF domain configuration. The star symbol depicts the BNPP location. The outermost boundaries denote the parent domain (D01, 25 km). D02 (5 km) and D03 (1 km) are the nested domains. (b) Zoom-in view of the innermost domain (D03) with shading giving model orography (m). The location of the BNPP is depicted by a star symbol. (c) Overview of instrumentation deployed at Barakah, United Arab Emirates.

184

185

Table 1: List of instrumentation collocated at Barakah nuclear power plant, parameters analyzed, and periods of data analysis.		
Instrument (Make and Model)	Analyzed variables	Analysis period
Visibility (Sentry™, 73000S)	Horizontal visibility	27 January - 27 April 2021
Fog monitor (Droplet Measurement Technologies, FM-120)	Liquid water content and particle size distribution	18 October 2021 - 16 March 2022
Portable weather station (LUFT, WS501-UMB smart weather sensor, WS100 smart disdrometer)	Air temperature, relative humidity, wind speed and wind direction	
Microwave radiometer (RPG-HATPRO; G5 series)	Air temperature and relative humidity profiles	
3D Ultrasonic anemometer	Three components of wind (u, v, w)	9 December 2021 - 25 May 2022



186 **2.3 Satellite and Reanalysis Products**

187 Geostationary satellite images are used to assess the spatial extent of the fog events. For this, the
188 Spinning Enhanced Visible and Infrared Imager (SEVIRI) instrument onboard Meteosat-10
189 (situated over 9.5° E) was utilized (Schmetz et al., 2002). The resolution is about 4 km and the
190 images are available every 15 minutes. Day and night-time RGB (red, green, blue) images are
191 created based on the EUMETSAT guidelines. The daytime natural color RGB (red, green, blue)
192 product images are created using the visible and near infrared channels as follows: NIR1.6 (red),
193 VIS0.8 (green) and VIS0.6 (blue). In these images, the fog appears as a white cloud during
194 daytime. In the night-time microphysical product, the red channel is the difference between 12.0
195 and 10.8 μm channels (linear stretch – 4 to 2 K), the green channel is the difference between 10.8
196 and 3.9 μm channels (linear stretch 0 to 10 K) and the blue channel is the 10.8 μm channel (linear
197 stretch 243 to 293 K). The fog appears as light green in this product. The principle of the night-
198 time RGB is that fog has a lower emissivity in the 3.9 μm channel than 10.8 μm (Cermak and
199 Bendix, 2007; Ellrod and Gultepe, 2007; Gultepe et al., 2017). This difference is captured in the
200 green channel in the RGB and generally makes it distinguishable from cloud or land surface.

201 In addition to in-situ measurements and Satellite data, we used ERA-5 reanalysis data from the
202 European Centre for Medium-Range Weather Forecasts (Hersbach et al., 2020) to present the
203 overall synoptic conditions during the fog events. The ERA-5 data set was selected because it
204 offers higher spatial resolution (0.25°, about 27 km) and temporal resolution (hourly) compared to
205 other reanalysis data sets. Additionally, ERA-5 has demonstrated superior performance in the
206 region, as shown in previous studies (Mahto and Mishra, 2019; Tahir et al., 2020; Taraphdar et al.,
207 2021).

208 **2.4 Numerical Modeling**

209 **2.4.1 Meteorological Model: WRF**

210 In this study, we use the Advanced Research Weather Research Forecasting (ARW) v4.2 model
211 (Skamarock et al., 2008), a largely used community mesoscale model developed by the National
212 Center for Atmospheric Research (NCAR), to simulate meteorological conditions around BNPP.
213 To better resolve local-scale atmospheric circulation around the nuclear site, we use the same WRF
214 model configuration as in Abida et al. (2022). The domain setup consists of three two-way
215 interactive telescoping nested domains centered on BNPP's location (23.9696° N, 52.2359° E)
216 with the respective resolutions of 25 km, 5 km, and 1 km as depicted in Fig. 1a. Forty-five
217 unequally spaced sigma-pressure vertical levels are used with approximately 11 vertical levels
218 below 1 km above ground level to capture the vertical structure of the fog. The innermost domain,
219 representing the study area, consists of 311 × 311 grid points and encompasses a region within a
220 radius of 150 km from BNPP. The physical parameterizations schemes used in all model domains
221 include RRTMG for shortwave radiation (Iacono et al., 2008), RRTM for longwave radiation



222 (Iacono et al., 2008), Kain-Fritsch cumulus (Kain, 2004), thermal diffusion land surface scheme,
 223 and WSM 3-class microphysics (Hong et al., 2006). This microphysics scheme includes three
 224 categories of hydrometeors: water vapor, liquid water (including cloud water and rain), and frozen
 225 water (including ice cloud and snow) The liquid water components and the frozen water are treated
 226 for temperatures above and below 0°C, respectively.
 227 Regarding planetary boundary layer (PBL) schemes that parametrize turbulent vertical fluxes of
 228 heat, momentum, and moisture in the PBL, we considered three local PBL schemes, MYJ (Janjić,
 229 1994), MYNN2.5 (Nakanishi and Niino, 2006), and MYNN3.0 (Nakanishi and Niino, 2006), and
 230 two nonlocal PBL schemes, YSU (Hong et al., 2006) and ACM2 (Pleim, 2007). Note that for
 231 stable or neutral conditions, the ACM2 scheme shuts off nonlocal transport and uses local closure.
 232 This approach helps to determine the sensitivity of PBL parameterization for fog simulation. It is
 233 worth mentioning that in WRF, some PBL schemes are tightly tailored to particular surface layer
 234 schemes. Table 2 summarizes these PBL schemes with their associated surface layer options.
 235

Table 2: WRF used PBL Schemes

PBL scheme	Closure type	Surface Layer scheme	Short description
MYJ	1.5 local	Monin-Obukhov (Janjic Eta) scheme	An improved local closure scheme based on Mellor-Yamada 1.5 order local scheme using the turbulent kinetic energy (TKE) model. It is suitable for stable flows, making it more appropriate for fog modeling, but it might underestimate vertical mixing.
MYNN2.5	1.5 local	Monin-Obukhov (Janjic Eta) scheme	An updated scheme, TKE-based with level 2.5 turbulent closure model. It provides improvements in the surface layer, by modifying the exchange coefficients and non-local terms, resulting in better performance under very stable conditions. It improves the mixing length scale which leads to better control of the inadequate growth of the convective boundary layer.
MYNN3.0	2.0 local	MYNN	Similar to MYNN2.5 but it runs at level 3.0 closure. With a more accurate representation of the boundary layer, it may show some ability to simulate radiation fog.
YSU	1.0 nonlocal	Revised MM5 Monin-Obukhov scheme	A non-local closure scheme with a counter-gradient flux for heat in the unstable boundary layer. It is often used for its simplicity and computational efficiency. It may produce an excessive vertical mixing during the evening that leads to too deep PBL height.
ACM2	1.0 nonlocal	Revised MM5 Monin-Obukhov scheme	A non-local closure scheme, which predicts the boundary layer height, with an enhanced mixing for the stable boundary layers. It has a counter-gradient term for heat and moisture, making it well-suited for deep convective situations, but may over deepen the PBL.

236



237 The choice of a PBL parameterization scheme can significantly impact the accuracy of fog
238 simulation (Chaouch et al., 2017; Chen et al., 2020; Lin et al., 2017; Nelli et al., 2020a; Temimi et
239 al., 2020b). PBL schemes are classified based on two factors: the order of the turbulence closure
240 and the use of local or nonlocal mixing approaches. Turbulence closure refers to the mathematical
241 approach used to represent the effects of small-scale turbulent motions on larger-scale atmospheric
242 variables. Local closure schemes estimate the turbulent fluxes based on the mean atmospheric
243 variables at each point on the model grid, or possibly their gradients. In contrast, nonlocal closure
244 schemes use multiple vertical levels to determine variables at a given point. This approach allows
245 for the consideration of the effects of turbulence at other levels of the atmosphere.

246 Meteorological analysis from the National Centre for Environmental Prediction (NCEP) Global
247 Forecast System (GFS) with a horizontal spatial resolution of 0.25° and with a time resolution of
248 3h were used to provide initial and boundary conditions to WRF experiments. Besides atmospheric
249 fields, time-varying analyzed SSTs (Sea Surface Temperature) within NCEP GFS were also
250 supplied to the model.

251 **2.4.2 Atmospheric Dispersion Model: FLEXPART**

252 In this study, we use the Lagrangian particle dispersion model, FLEXPART-WRF (Brioude et
253 al., 2013), a widely used model for simulating atmospheric and deposition processes at various
254 spatial scales, ranging from small-scale dispersion of pollutants from power plant stacks to long-
255 range transport applications (Bahreini et al., 2009; Cooper et al., 2010). In addition to transport
256 and turbulent diffusion, the model considers radioactive decay and simulates both dry and wet
257 deposition of aerosols and gasses. The model works by computing trajectories of a large number
258 of small parcels of air containing initial concentrations of the species. These air parcels are then
259 advected downstream, subject to the unsteady velocity field, turbulence characteristics, turbulent
260 diffusion, as well as dry and wet deposition processes.

261

262 We recall that, in FLAXPART, the wet deposition is calculated based on the precipitation rate by
263 treating separately the in-cloud and below-cloud scavenging processes (Stohl et al., 2005). In
264 contrast the dry deposition velocity is calculated using the electric resistance method (Seinfeld et
265 al., 1998). The gravitational settling velocity component in the dry deposition parametrization for
266 a particle is given by

$$267 \quad v_g = g\rho_p d_p^2 C_{cun} / 18\mu \quad (1)$$

268

269 where ρ_p and d_p^2 are the particle density (kg m^{-3}) and diameter (m), respectively, μ is the dynamic
270 viscosity of the air ($\text{kg m}^{-1} \text{s}^{-1}$), C_{cun} is the Cunningham slip-flow correction, and g is the
271 acceleration of gravity (9.81 m s^{-2}).

272

273 Foggy atmospheric conditions can lead to the entrainment of radionuclides in water droplets,
274 which can then be deposited on earth's surface when the fog comes in contact with it. Additionally,



275 dry aerosols serve as Cloud Condensation Nuclei and can then grow by condensation of water
 276 vapor (Seinfeld et Pandis, 1998) leading to droplets prone to settle as a result of gravitation and
 277 turbulent impaction on obstacles. The coalescence process doesn't act on the released
 278 radionuclides, but it affects the size distribution of the fog droplets.

279

280 To account for the fog deposition processes as an additional scavenging agent in our dispersion
 281 simulation, we slightly modified the gravitational settling in equation 1 by adding to it an
 282 additional thresholding term. In a given model grid cell, if the LWC (averaged over the lower three
 283 model levels) is found to be greater than 0.1 g m^{-3} , then this term is set to the value of 3 cm s^{-1} , as
 284 a representative value of fog deposition rate around Barakah site. Otherwise, it is set to zero. The
 285 minimal threshold value of 0.1 g m^{-3} to determine whether a grid cell is foggy or not was chosen
 286 based on trial simulations which showed that the WRF model tends to overestimate the near-
 287 surface liquid water content when compared to LWC observations at BNPP (see later, Fig. 11a).

288 2.5 Detection of fog over experiment site

289 Fog is a meteorological condition where horizontal visibility becomes less than a conventionally
 290 accepted threshold of 1000 m due to the presence of water droplets. In this study, fog events are
 291 detected based on the horizontal visibility measured at a height of 10 m. First, all time-steps where
 292 horizontal visibility is less than or equal to 1 km are labeled as potential fog events (Fonseca et al.,
 293 2023; Mohan et al., 2020; Nelli et al., 2022; Temimi et al., 2020a). Afterwards, a visual inspection
 294 of 15-minute SEVIRI fog RGB images is conducted to confirm the formation of fog on the selected
 295 dates and times. Additionally, cloudy or rainy conditions are filtered out using the 30-min merged
 296 IR brightness temperature data from geostationary satellites (Nelli et al., 2021b; Rao et al., 2013;
 297 Reddy and Rao, 2018). A detailed list of each fog occurrence, including the date, time, duration,
 298 and minimum horizontal visibility during each fog event is given in Table 3.

299

Table 3: Fog occurrence timings (onset, dissipation, and duration) at Barakah and minimum horizontal visibility for each of the 12 fog events.					
S.No.	Start Date	Fog occurrence timings			Minimum horizontal visibility (m)
		Onset	Dissipation	Duration (hour)	
1	2021-01-29	04:32 LT	05:39 LT	01:01	241
2	2021-02-04	00:32 LT	08:03 LT	02:04	154
3	2021-02-05	02:35 LT	08:03 LT	05:27	120
4	2021-02-13	06:06 LT	08:05 LT	00:31	130



5	2021-02-16	00:28 LT 06:38 LT	04:40 LT 08:56 LT	04:12 02:18	90
6	2021-02-17	00:22 LT	06:14 LT	01:55	165
7	2021-11-23	05:01 LT	09:10 LT	03:53	102
8	2022-01-27	02:43 LT	08:02 LT	04:03	261
9	2022-02-04	02:01 LT	09:20 LT	06:15	198
10	2022-02-11	06:00 LT	06:31 LT	00:32	200
11	2022-02-24	04:06 LT	09:33 LT	04:07	44
12	2022-02-25	00:28 LT	00:54 LT	00:13	253

300 Microphysics and dynamics for these 12 fog events are presented in sections 3 and 4. In section
 301 5, the impact of the long-lasting fog event on February 16 2021 on ground deposition of radioactive
 302 materials in case of an accidental radioactive release at Barakah Nuclear Power Plant (BNPP) is
 303 presented.

304 2.6 Fog deposition flux calculations

305 In this section, we describe how the total vertical fog water flux between the surface and the
 306 atmosphere and the fog deposition velocity are estimated using data from the fog monitor sampler
 307 and ultrasonic anemometer installed at BNPP.

308

309 Before calculating any quantity related to fog deposition, we first pre-processed fog monitor data
 310 for all recorded fog events at the site. We recall that the fog monitor provides information on LWC,
 311 the number of water droplets per bin droplet size, and the Median Volume Diameter (MVD) every
 312 1 second. The data were re-sampled to 1-minute frequency. The concentration number $N_i(t)$ per
 313 size bin for each time step t ($\#cm^{-3}$) is calculated by

$$314 \quad N_i(t) = \frac{n_i(t)}{dw_i * SV(t)} \quad (2)$$

315

316 where $n_i(t)$ and $SV(t)$ are the count of droplets in size bin i and the sampling volume in cm^3 at
 317 time t , respectively; dw_i is the width of the size bin i in logarithmic scale calculated as $dw_i =$
 318 $\log(u_i/l_i)$, with u_i and l_i being the upper and lower bounds of the size bin i , respectively. Based
 319 on the assumption of spherical shape of fog water droplets, the liquid water content LWC_i ($kg\ m^{-3}$)
 320 available within the bin droplet size i at time t is given by:

321

$$322 \quad LWC_i(t) = \frac{1}{6} \pi d_i^3 N_i(t) dw_i \rho_w \quad (3)$$



323

324 where ρ_w is the density of water (kg m^{-3}), d_i is the geometric mean diameter (μm) for each droplet
 325 size class. As in Tav et al. (2018), we calculated the concentration number density ($\rho_{nc}(i, t)$), and
 326 the mass density ($\rho_{lwc}(i, t)$) of each size bin i and at each time step t as follows:

327

$$\rho_{nc}(i, t) = \frac{1}{dw_i} \left(\frac{N_i(t)}{\sum_{i=1}^{30} N_i(t)} \right)$$

$$\rho_{lwc}(i, t) = \frac{1}{dw_i} \left(\frac{LWC_i(t)}{\sum_{i=1}^{30} LWC_i(t)} \right)$$

328

329 Note that the total water flux in the fog is a combination of the turbulent liquid flux, gravitational
 330 settling of droplets, water condensation and an advection component. Yet, the last two processes
 331 lead to flux magnitudes at least six orders lower than the first two, as reported by Spirig et al.
 332 (2021) and Eugster et al. (2006). In addition, the determination of the liquid water flux due to the
 333 advection would require the installation of several fog monitors around the nuclear site, which is
 334 beyond the scope of this study.

335

336 Thus, in this study, the total flux of liquid water in the fog ($\text{kg m}^{-2}\text{s}^{-1}$), LWF_{total} , is expressed only
 337 by the sum of the turbulent and gravitational settling components:

338

$$LWF_{total} = LWF_{turb} + LWF_{grav} \quad (4)$$

340

341 The gravitational settling flux, LWF_{grav} is calculated based on Stoke's law for settling velocity
 342 (Beswick et al., 1991):

343

$$v_s = gd^2(\rho_{water} - \rho_{air})/18\eta_{air} \quad (5)$$

344

345 where g is the gravity acceleration (9.81 m s^{-2}), η_{air} is the dynamic viscosity of the air ($\text{kg m}^{-1}\text{s}^{-1}$),
 346 d is the droplet diameter (μm), ρ_{water} and ρ_{air} are respectively the water and air densities (kg m^{-3}).
 347 The settling velocity v_s (m s^{-1}) is calculated for each droplet size class i and multiplied by the
 348 liquid water content within this size class, LWC_i . The total gravitational settling flux is then the
 349 sum of the interval fluxes over all droplet sizes:

350

$$LWF_{grav} = \sum_i v_{s,i} LWC_i \quad (6)$$

351

352 Note that the gravitational settling process is more efficient for water droplets of larger sizes,
 353 typically greater than $10 \mu\text{m}$.



354

355 In contrast, the turbulent deposition process which depends on the turbulent exchange between the
356 atmosphere and the surface, is more effective for small water droplets because they can more easily
357 follow the chaotic, turbulent flow of the air and remain suspended in it for longer periods of time.
358 The liquid water turbulent flux LWF_{turb} is calculated based on the Eddy Covariance (EC) technique.
359 First, a double rotation correction was used to align the wind horizontal component (u) with the
360 mean wind to obtain a zero average for the other wind components v and w (Rao and Reddy, 2019).
361 The EC framework, in which co-located measurements from a fog monitor sampler and a sonic
362 anemometer are combined, is widely used to derive the turbulent liquid water flux (Beswick et al.,
363 1991; Degefie et al., 2015; Klemm and Wrzesinsky, 2007; Kowalski and Vong, 1999; Spirig et
364 al., 2021; Thalmann et al., 2002; Westbeld et al., 2009).

365

366 The turbulent vertical flux is subsequently determined as the covariance between the vertical wind
367 speed (w ; m s^{-1}) and LWC time series:

$$368 \quad LWF_{turb} = \overline{w'LWC'} \quad (7)$$

369

370 The overbar indicates a 15 min temporal average and the prime indicates the deviation of each
371 component from its 15 min mean.

372

373 The time-dependant settling velocity v_s is calculated as the ratio of the gravitational settling flux
374 to the 15 min averages of liquid water content:

375

$$376 \quad v_s = -\frac{LWF_{grav}}{LWC} \quad (8)$$

377

378 Note that we can also estimate this quantity directly by applying Stoke's sedimentation velocity
379 formula using as the droplet diameter size the median diameter volume (MDV) data from the fog
380 monitor. Both approaches have been found to lead to very similar results (results not shown).

381

382 Similarly, the fog droplet net deposition velocity, v_d , is determined by calculating the ratio of the
383 total fog water flux to the 15-min averages of liquid water content using the following equation:

$$384 \quad v_d = -\frac{LWF_{total}}{LWC} \quad (9)$$

385

386 Note that a positive sign of v_d indicates a downward flux. It should be noted that a net gain of
387 water deposition on the surface is not necessarily all-time guaranteed despite the presence of fog.
388 Tav et al. (2018) by using a weighing measurement setup found that among other factors, the
389 deposited fog water depends significantly on the type of surface.



390 **3. Fog Microphysics and dynamics**

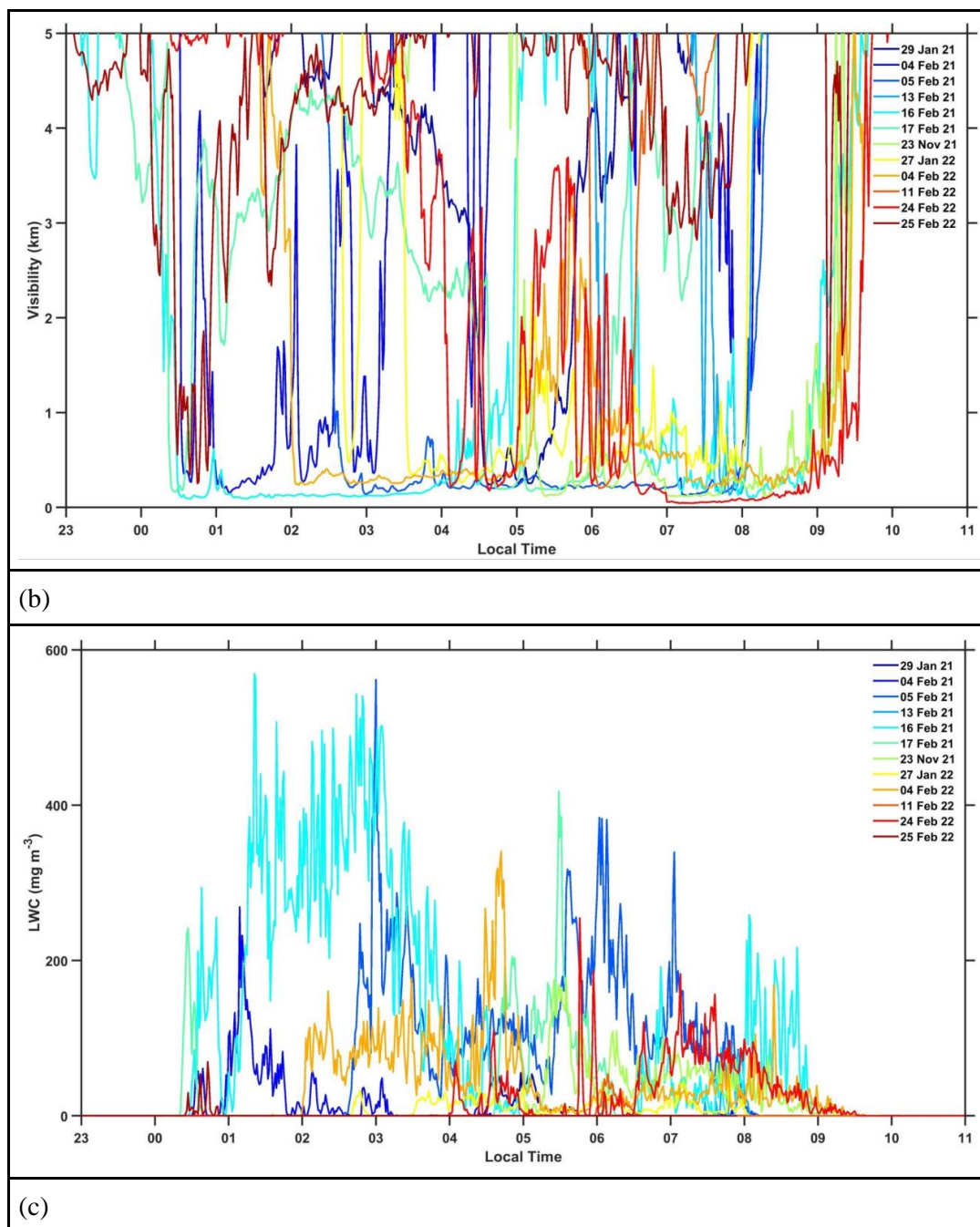
391 **3.1 Fog microphysics**

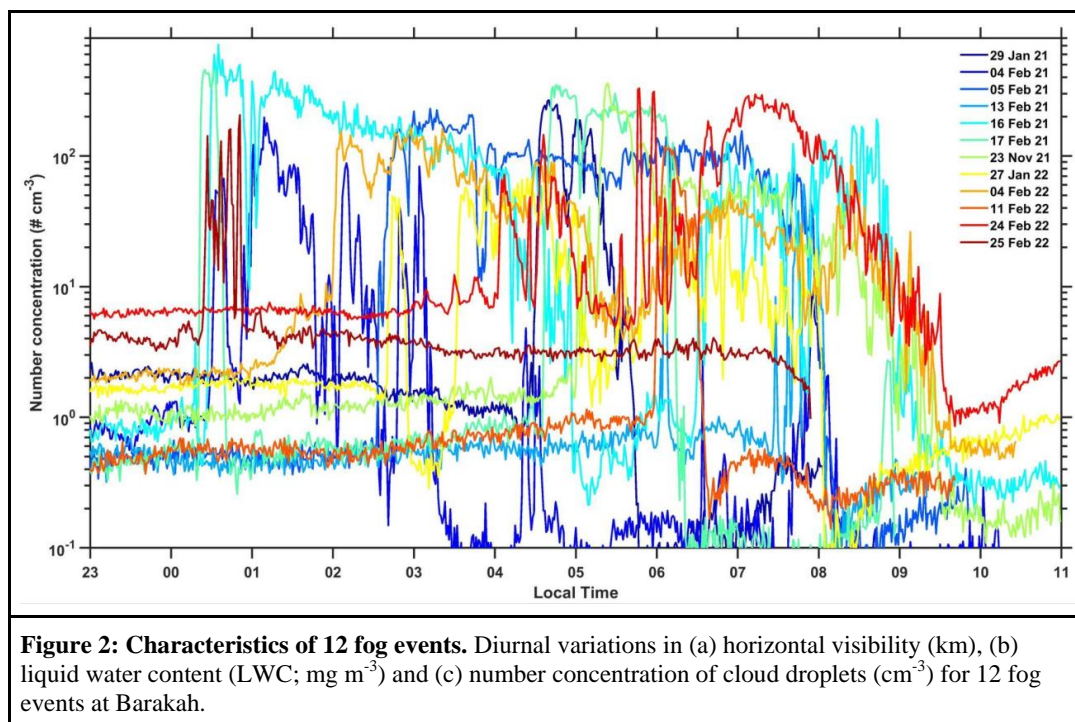
392 The microphysics of fog were analyzed based on observations of 12 fog events that occurred
393 during the winter seasons of 2021 and 2022. Diurnal variations in horizontal visibility, liquid water
394 content, and number concentrations were studied for each of the 12 fog events, as depicted in Fig.
395 2.

396 The onset and maturation of fog at Barakah were found to occur between 0-4 LT and 6-7 LT,
397 respectively, as shown in Table 3 and in Fig. 2a. Our results are consistent with the diurnal
398 variations in fog occurrence reported by Nelli et al. (2022) at the Barakah site. Nelli et al. (2022)
399 used long-term meteorological data from a weather station for their study. Additionally, our
400 findings are in line with Weston et al. (2021a) report on fog occurrence at Abu Dhabi International
401 Airport, which is a coastal location in the UAE. Weston et al. (2021a) analyzed the meteorological
402 aerodrome report (METAR) data to arrive at their conclusions. Interestingly, the onset of fog at
403 Barakah is more swift than that in fog events at Abu Dhabi (Temimi et al., 2020), both being
404 coastal sites. Perhaps the radiative cooling is more pronounced given the more arid landscape as
405 opposed to the urban environment in Abu Dhabi. Regarding the fog microphysical properties, we
406 observed that, similar to the abrupt decrease in horizontal visibility, both the LWC and number
407 concentration also increase abruptly. The mean and median of LWC when the horizontal visibility
408 reduces to less than or equal to 1 km are 150 and 170 mg m⁻³, respectively. Interestingly, the LWC
409 and number concentrations for the 04 February 2022 event are relatively lower than those for the
410 16 February 2021 fog event, despite a similar fog duration. This difference is further discussed in
411 section 3.2, along with the thermodynamics parameters obtained from weather stations and the
412 measurements collected by the microwave radiometer.

413

(a)





414

415

416 To better understand the droplet size distribution (DSD), the number concentration ($\# \text{ cm}^{-3}$,
 417 hereafter, N_c) in each bin droplet size is averaged over the duration of each fog event and
 418 normalized by the width of the size bin in the logarithmic scale. Fig. 3a indicates that all the fog
 419 events exhibit the same shape of a bimodal distribution, with peaks about 4.5 and 23 μm . The DSD
 420 of the composite of all fog data with visibility less than or equal to 1 km also shares the same
 421 shape. The ratio of the number concentration in the first mode to the second mode is almost 5,
 422 indicating that the proportion of small droplets is significantly larger than the proportion of large-
 423 size droplets in the fog.

424

425 Bimodal distributions of fog water droplet sizes are common as reported by numerous studies in
 426 the literature (Gultepe and Milbrandt, 2007; Westbeld et al., 2009; Weston et al., 2022; Ghude et
 427 al., 2023). Note that the shape of the DSD could also be, in part, influenced by the type of the
 428 condensation nuclei available at this semi-arid coastal site. The bimodal distribution is a result of
 429 the coexistence of two distinct populations of particles. The first mode, 4.5 μm corresponds to
 430 smaller droplets which are formed through condensation of water vapor during the initial stage of
 431 the fog. The second mode, 23 μm corresponds to larger droplets which are mainly formed through
 432 the coalescence and collision of smaller droplets during the intermediate and mature stages of the
 433 fog as addressed in the subsequent sections. Interestingly, the bimodal distribution is also observed
 434 in LWC distribution as a function of droplet sizes with a more broadening mode at 4.5 μm and a



435 marked peak at $25 \mu\text{m}$ as highlighted in Fig. 3b. The DSD mode at $4.5 \mu\text{m}$ has a very minor
436 influence on the LWC and most likely formed at the onset stage of the fog. This result reveals that
437 despite the large proportion of small particles with diameters less than $5.5 \mu\text{m}$ in the fog, the largest
438 contribution to the LWC originates essentially from medium to large-size droplets between 10 and
439 $35 \mu\text{m}$. The twelve fog cases reveal clear differences between them in terms of the variability of
440 the LWC and N_c values (Fig. 4a), even though almost all of them are of the radiation fog type.
441 LWC and N_c range from 10 to 600 mg m^{-3} and 10 to $480 \# \text{ cm}^{-3}$ respectively, while MVD ranges
442 from 2.11 to $30 \mu\text{m}$ (Fig. 4b). Overall, and especially for long-lasting fog events (longer than 90
443 min), we observe that the maximum values for N_c , LWC and MVD obtained in this study tend to
444 be higher compared to other values reported in the literature, in particular for the values reported
445 for continental fog events (Boutle et al., 2018; Egli et al., 2015; Formenti et al., 2019; Gultepe and
446 Milbrandt, 2007; Mazoyer et al., 2019). However, it should be noted that these ranges are sensitive
447 to the temporal frequency at which the data is re-sampled (1 min in this study).

448

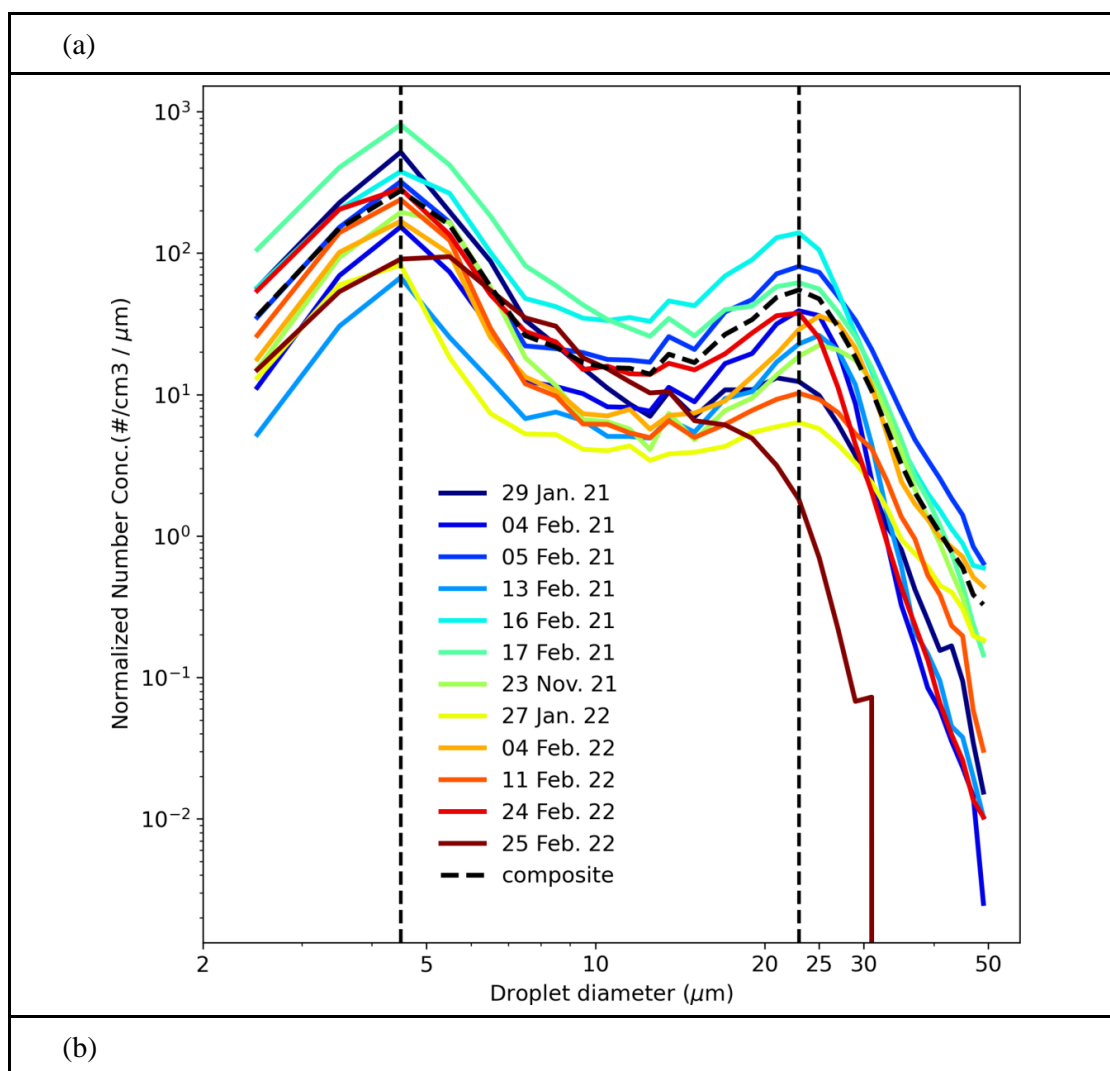
449 In addition, the analysis of the spread of MVD data for each fog event, as shown by the box plots
450 in Fig. 4b, indicates that on average the MVD ranges from 20 to $26 \mu\text{m}$ in almost all the cases,
451 except for the fog event observed on February 25, 2022, which has the smallest median MVD of
452 about $5 \mu\text{m}$. This fog event has the shortest lasting time of 13 minutes among all other fog events
453 and based on SEVIRI Fog RGB images (Fig. A3), is most likely a remnant from a fog formed over
454 the sea and advected by the winds toward the site when it was detected. Interestingly, we notice
455 that the fog event recorded on 16 February 2022 shows the lowest variability amongst all other
456 fog cases with a minimum interquartile range (IQR) of $2.5 \mu\text{m}$ and median MVD of $24 \mu\text{m}$. We
457 observe that the lower and upper quartiles for most fog cases are between 20 and $28 \mu\text{m}$. This
458 suggests that radiation fogs occurring during the winter at this hyperarid coastal site tend to have
459 larger water droplets. Note that the excess of the moisture content and the warm air available at
460 the site also enhance the growth in size of the droplets, as warm air can hold more moisture.

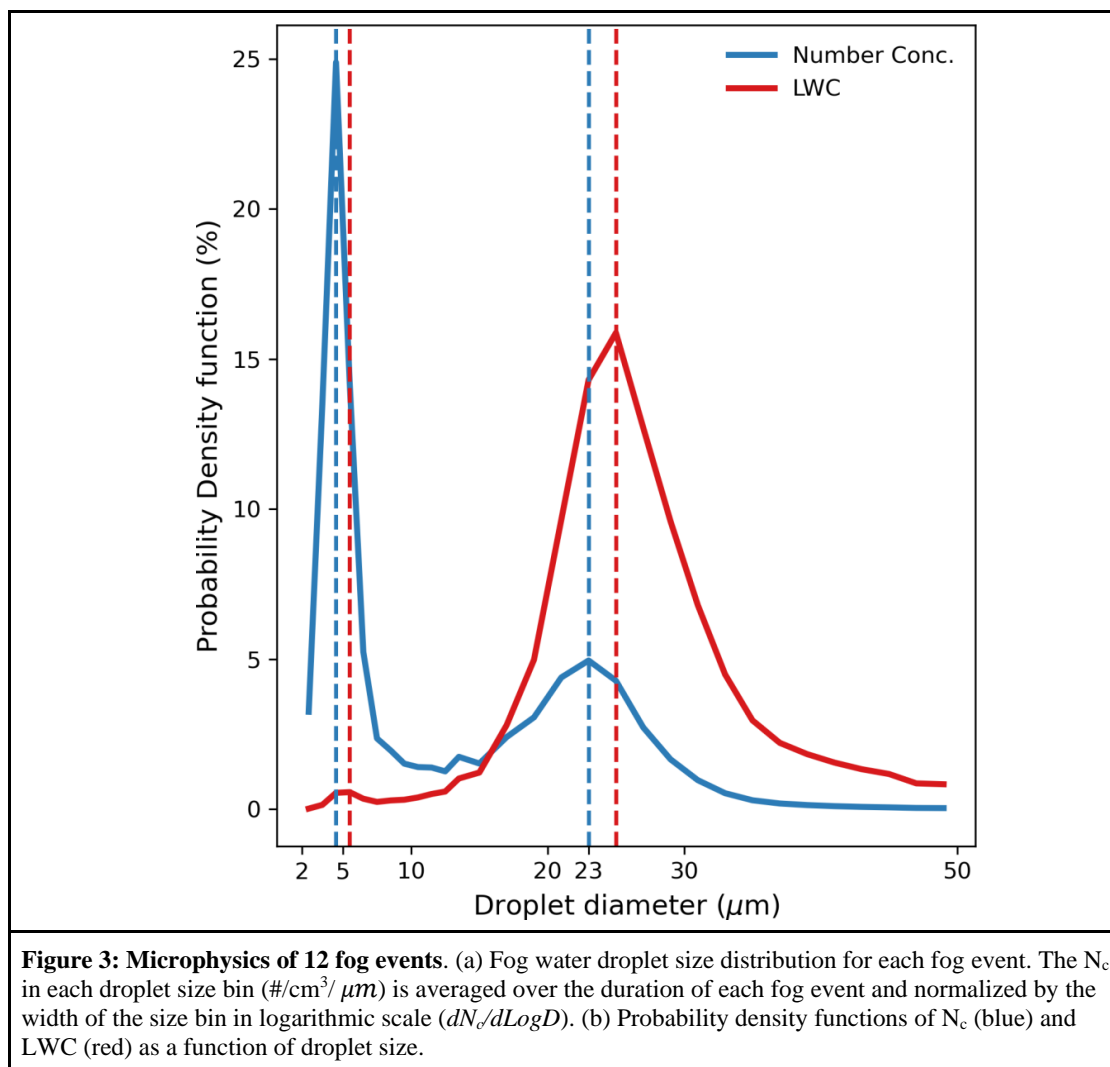
461

462 The relationship between the LWC and N_c in fog is complex and depends on various factors,
463 including ambient temperature, humidity, and the quantities of aerosol particles that can serve as
464 nuclei for fog droplet formation. In general, when the LWC increases, the N_c also increases.
465 However, at some point, the N_c might start to decrease due to coalescence resulting in larger
466 droplets, which in turn may decrease in number due to gravitational settling. Also, this relationship
467 can vary depending on the droplet size distribution. To shed some light on this relationship we first
468 examined the temporal variation of LWC as a function of the droplet sizes, and calculated the
469 probability density functions of LWC and N_c for the twelve fog events. It was found that the results
470 for almost all fog events are very similar to each other and therefore lead to the same primary
471 conclusions. Thus, we only present here the results of the fog event observed on February 16,
472 2021, which is an interesting case with a longer duration and associated with a greater reduction
473 in horizontal visibility (see Table 3). Figure 5a shows the time-variation of LWC per size bin as
474 well as the integrated LWC. The fog event on 16 February 2021 started at 00h28 (LT) and lasted

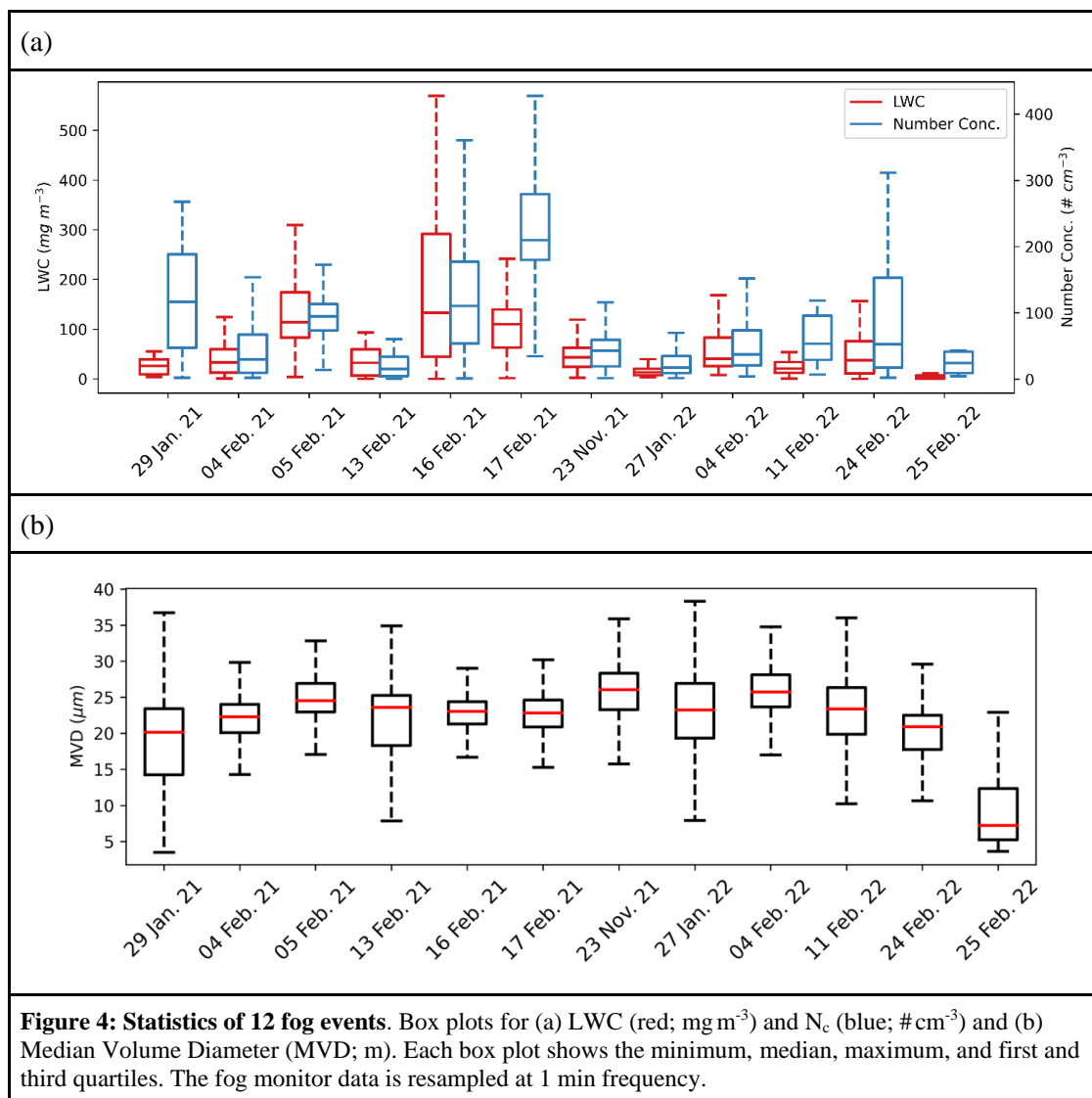


475 4:12 hours till 04h40 (LT). The LWC then decreased drastically for about 1.5 hours before starting
476 to increase when a second fog patch moved in at 06:38 (LT) and lasted for 2:18 hours. The
477 colormap indicates that LWC reaches its maximum values during the fog maturation phase for
478 droplet sizes between 20 μm and 30 μm . This again corroborates that the larger-size droplets in
479 the fog have the largest contribution to the LWC compared to the smaller-size droplets.
480





481
482
483
484
485
486
487
488
489
490



491

492

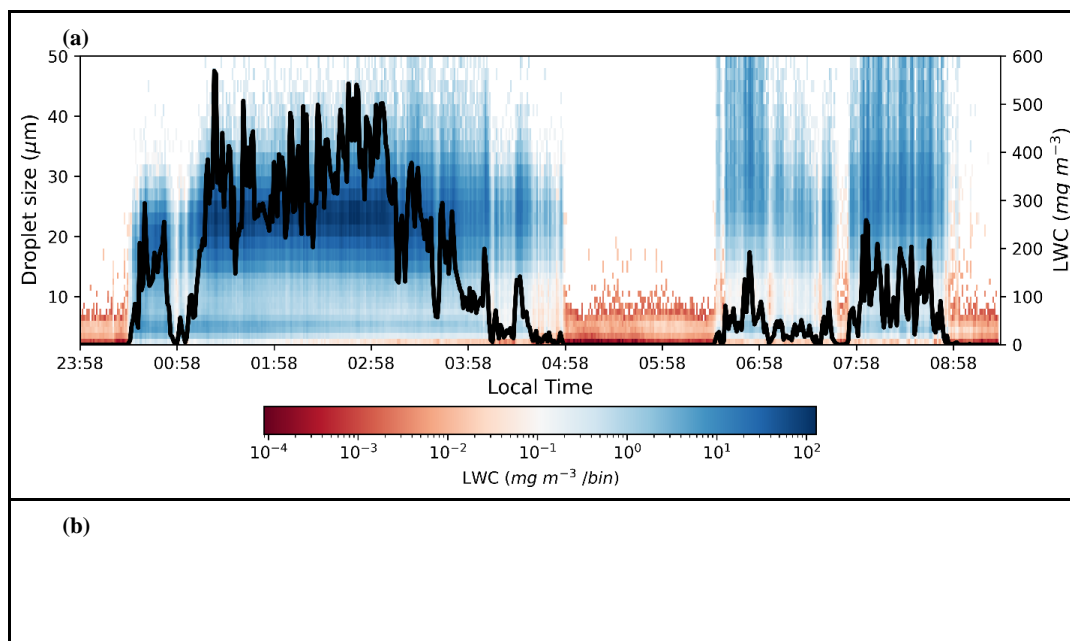
493 Figure 5b shows calculated mass and number probability densities for four typical droplet size
 494 ranges: $1\text{-}5 \mu\text{m}$, $5\text{-}10 \mu\text{m}$, $10\text{-}20 \mu\text{m}$ and $20\text{-}50 \mu\text{m}$, which will determine the contribution of each
 495 droplet size class to the total number concentration per cm^3 and to the total mass of liquid water
 496 per m^3 . This will help to explore the size distribution of fog droplets and its contribution to the
 497 liquid water content. Interestingly, we observe that at the onset of the fog, the droplet sizes between
 498 1 and $5 \mu\text{m}$ and between 5 and $10 \mu\text{m}$ represent respectively 60-80% and 20-40% of the total
 499 number of droplets, and between 40 to 60 % of the total mass of liquid water. This suggests that
 500 the LWC is more controlled by smaller to medium droplets at the onset phase. In addition, during

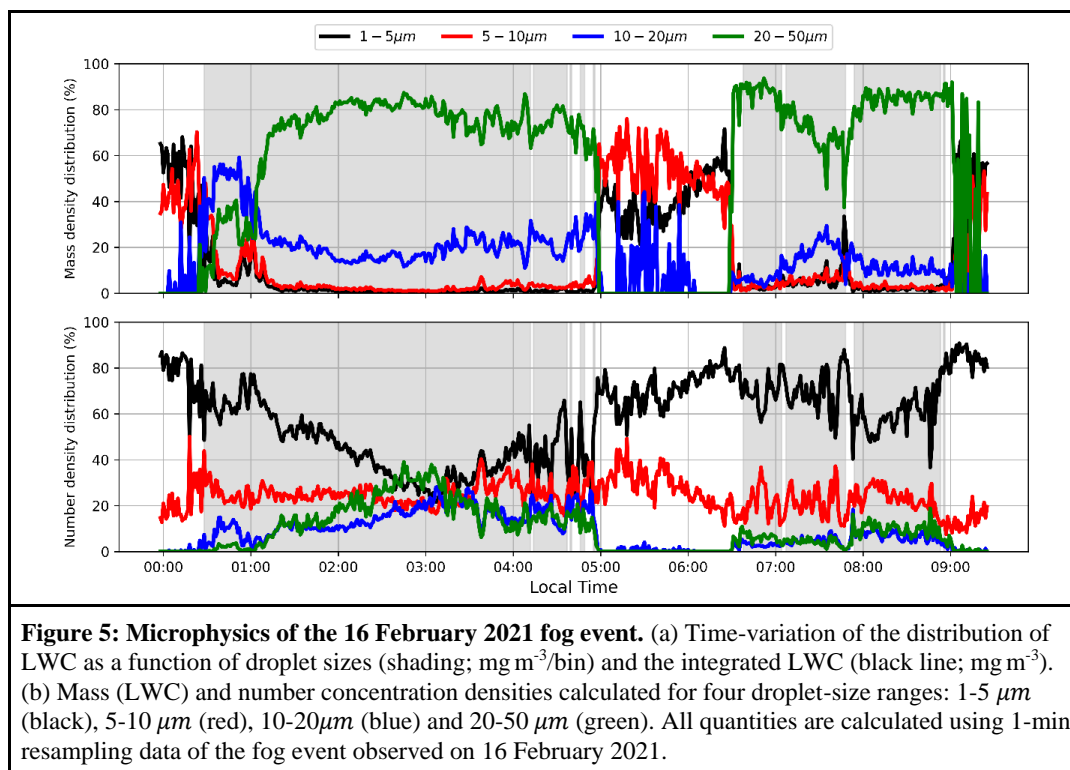


501 the mature stage, we notice that the percentage of droplets between 1 and 5 μm of the total number
502 density gradually decreases until about 03:15 (LT) when it begins to increase. However, the
503 opposite is observed for larger droplets particularly between 20 and 50 μm . Note that large droplets
504 represent on average less than 20% of the total number of droplet density. This indicates that, at
505 the onset and mature stages of the fog, the proportion of smaller droplets is significantly higher
506 than that of larger droplets. The number density of droplets between 5 and 10 μm does not change
507 significantly and fluctuates on average mostly between 20 and 25% in the mature stage. This
508 reveals that during the mature phase of the fog, the larger droplets are formed mainly by collision-
509 coalescence process which is more efficient for smaller droplets with sizes between 1 and 5 μm .
510 Once formed, the larger droplets can settle to the surface due to gravitational sedimentation and
511 turbulence, reducing the liquid water content in the air. Combined, droplets between 10 and 20
512 μm and 20 and 50 μm account for up to 90% of the condensed water in the air. In particular, the
513 very large droplets (20 and 50 μm) alone represent up to 80% of the total mass in the mature stage.
514 This supports the claim that higher LWC values are primarily attributed to the presence of a
515 sufficient number density (between 20-40%) of large droplets in the fog. This result is in perfect
516 agreement with Tav et al. (2018), who studied fog events in France and came to the same
517 conclusion.

518

519





520

521 3.2 Atmospheric thermodynamics during fog events

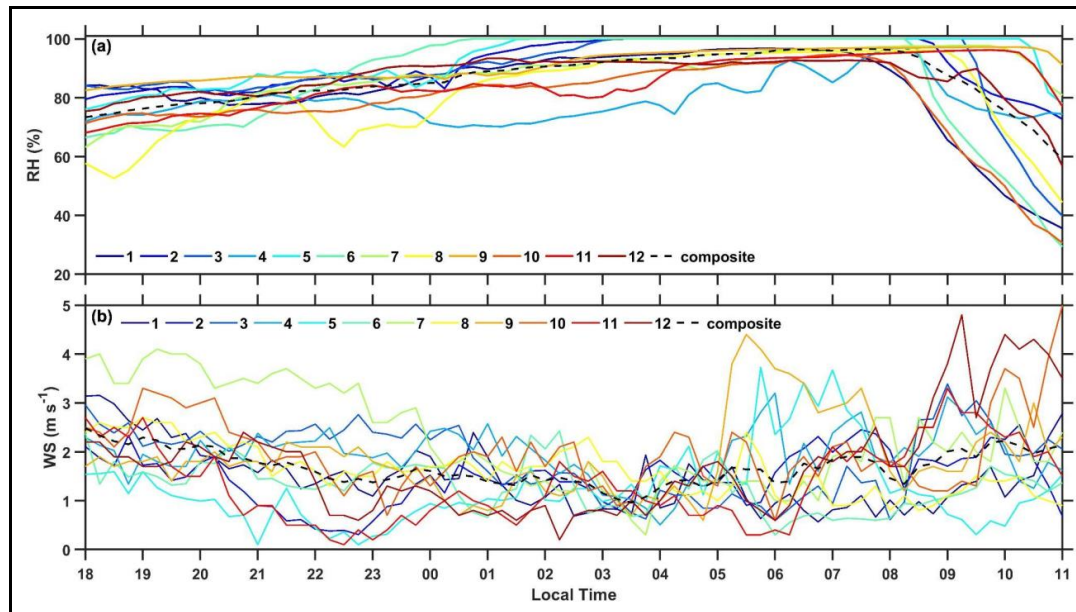
522 The thermodynamics and dynamics of fog are analyzed based on collocated weather station and
 523 microwave radiometer data. Diurnal variations in relative humidity and wind speed are studied for
 524 each of the 12 fog events, as depicted in Figs. 6a-b. The mean relative humidity and wind speed at
 525 the onset of fog for the 12 cases are 94% and 3 m s^{-1} , respectively, which are consistent with the
 526 threshold values used by Nelli et al. (2022) for detecting fog occurrence over Barakah using
 527 weather station data. For the fog events on 16 February 2021 and 04 February 2022 the wind speed
 528 exceeded 3 m s^{-1} in the middle of the fog event. During this time, an increase in horizontal visibility
 529 ($> 1 \text{ km}$) and a sudden decrease in LWC and number concentrations were measured Figs. 2a-c.

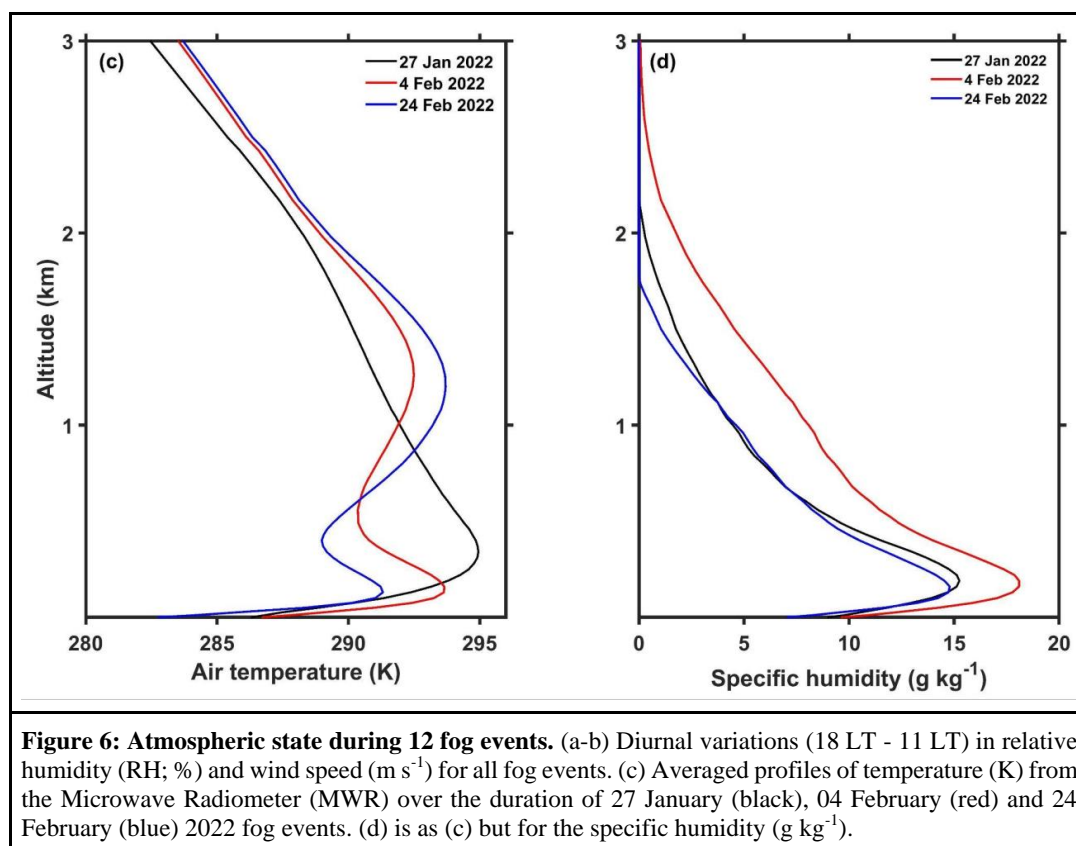
530 To investigate the factors that contribute to the differences in LWC and number concentration
 531 between the February 2021 and 2022 fog events, we analyzed the temperature and specific
 532 humidity profiles retrieved from the microwave radiometer data. Fig. 6c shows that the February
 533 2022 fog events were associated with double temperature inversions on 04 and 24 February, and
 534 a strong temperature inversion on 27 January. Double temperature inversions, similar to those
 535 observed during the February 2022 fog events, were also detected in the ceilometer backscatter
 536 profiles (Francis et al., 2023) prior to the onset of fog (elevated second layer) (Fig. A2). On the



537 other hand, the 16 February 2021 fog event occurred in a relatively less stable atmosphere with a
538 single temperature inversion. The strength and depth of temperature inversion for all 12 fog events
539 are shown in Fig. A1. It is concluded that the inversion depth and strength play a crucial role in
540 determining the moisture pumping to the fog layer and hence the growth of new droplets, which
541 affects the liquid water content. Other factors, such as the advection of air mass and descending of
542 stratus, can also influence the LWC and N_c . However, the differences in the temperature and
543 humidity profiles, as well as the strength and depth of temperature inversion, are likely the primary
544 contributors to the observed differences in LWC and N_c between the February 2021 and 2022 fog
545 events. It would be interesting to further investigate the roles of these meteorological factors in fog
546 formation and evolution using more detailed observations and modeling simulations in future
547 studies. The vertical velocity at 700 hPa obtained from ERA-5 data (not shown) indicates descent
548 on 04 and 24 February and weak ascent on 27 January 2022, which also supports the influence of
549 large-scale descent motion on the fog formation and growth. However, more detailed analyses of
550 the atmospheric dynamics and thermodynamics are needed to fully understand the complex
551 interplay between various meteorological factors, aerosols composition and fog properties.

552





553

554 An analysis of the large-scale circulation patterns for the 12 fog cases, based on the ERA-5 data,
 555 indicates the following: (i) a low-pressure system over the eastern Mediterranean extending into
 556 Iraq and northern Saudi Arabia; (ii) a ridge over the southeastern Arabian Peninsula; (iii) a strong
 557 southwesterly flow between the two, advecting moisture from the Red Sea into Iran and the
 558 northern Arabian Gulf; (iv) some of the moisture in the northern Gulf is brought into the UAE by
 559 the counterclockwise circulation of the ridge; and (v) weak near-surface wind speeds that favor
 560 the occurrence of fog (Fig. A4). The anomalies show the advection of drier air from continental
 561 Asia into the southeastern Arabian Peninsula (drier air aloft promotes the formation of fog), while
 562 the wind vector anomalies oppose the background flow, indicating more quiescent conditions.
 563 These large-scale patterns are consistent with those that favor consecutive fog events in the UAE,
 564 as discussed in Fonseca et al. (2022), resembling those of the prevailing cluster #1.

565 4. Fog deposition

566 In this section, we present fog droplet deposition velocities and liquid water deposition fluxes
 567 calculated based on the EC framework for three fog events measured at the Barakah nuclear site



568 on January 27, 2022, February 4, 2022, and February 24, 2022. Note that it was not possible to
569 apply the EC technique to the other fog events prior to these dates because the ultrasonic
570 anemometer was not yet installed at BNPP.

571

572 Figure 7a shows the temporal variation of the gravitational liquid water flux and the settling
573 velocity computed for the fog case of February 16, 2021. As expected, we observe that these two
574 quantities are positively correlated when accounting for the sign convention as given by equation
575 (6). Higher magnitudes of liquid water flux due to the sedimentation process are attributed to larger
576 water droplets with higher sedimentation velocities. The microphysical mechanisms of
577 condensation, coalescence, and evaporation impact the number density and size distribution of
578 water droplets in the fog, which in turn affect the rate of gravitational settling during the duration
579 of the fog event. Therefore, to investigate the change in gravitational sedimentation rate over time,
580 we calculated the time-series for the twelve fog events. We calculated settling velocities every 5
581 minutes, discarding the values associated with visibility greater than 1 km (Fig. 7b). The calculated
582 gravitational sedimentation velocity for each fog event exhibits a temporal variability which is
583 most likely determined by the time-variation of the number density of the largest water droplets in
584 the fog. In addition, we observe that the values of the settling velocities are in the range of 0.1 to
585 3.5 cm s⁻¹. To determine how the distribution of LWC values is related to the gravitational
586 sedimentation rate, we binned the LWC values over 6 bins of size 100 mg m⁻³ using the composite
587 data from the different fog events. Thus, for each LWC aggregate, we computed the number of
588 water droplets and the maximum, minimum, median, mean, and standard deviation values of the
589 settling velocities, as summarized in Table 4. This calculation confirms that a direct relationship
590 between LWC in the fog and the gravitational settling rate is not necessarily warranted.

591

592 Figures 8a-b show respectively the temporal variation of the fog droplet deposition velocity (v_d ;
593 equation (9)) and the associated turbulent kinetic energy flux ($\overline{w'^2}$) every 15 min for these three
594 fog cases. Notice that a positive sign of the fog deposition velocity indicates that more fog droplets
595 are depositing onto the surface than are being re-entrained into the air. This results in a net gain in
596 fog deposition for the surface. In contrast, a negative sign of the fog deposition velocity represents
597 a net loss of fog deposition for the surface.

598

599 First, we observe that the fog deposition velocity for the January 27, 2022 case exhibits more
600 variability with higher magnitude compared to the other two cases. These two latter show
601 particularly lower values of v_d ranging from 0.1 to 5 cm s⁻¹. It is noteworthy that the turbulence
602 energy associated with the fog of January 27, 2022, is significantly higher compared to the other
603 two fog events. This indicates that the deposition of fog droplets due to the turbulence mechanism
604 for January 27, 2022 is larger compared to the other cases. Moreover, it is interesting to note that
605 v_d for the January 27, 2022 fog event shows a maximum value of almost 40 cm s⁻¹, associated
606 with a peak of the turbulent kinetic energy flux occurring 30 min earlier as shown in Fig 8b. The
607 averaged values of v_d over the duration of each fog event for the three cases are respectively, 7.8



608 cm s^{-1} for January 27, 2022, 3.5 cm s^{-1} for February 4, 2022 and 2.1 cm s^{-1} for February 24, 2022.
609 These calculated values are of the same order of magnitude with the fog deposition velocity values
610 reported by Tav et al. (2018), in particular with those calculated for the bare soil category. Yet,
611 they found that the calculated fog deposition velocities for cypress and grass as deposition surfaces
612 are significantly high, with average values of 16 cm s^{-1} and 40 cm s^{-1} respectively.

613

614 Figure 9 shows the 15-min variation of the turbulent liquid water flux, LWF_{turb} , the gravitational
615 settling liquid water flux, LWF_{grav} and the total liquid water flux, LWF_{total} , defined by equations
616 (4), (6) and (7), calculated for 27 January 2022, 04 and 24 February 2022 fog cases. Additionally,
617 the temporal variation of the total liquid water flux in the fog with respect to the droplet sizes is
618 also shown. Calculated fluxes are standardized to $\text{mg m}^{-2} \text{ s}^{-1}$. Note that a negative sign of the total
619 liquid water flux means that there is a net flux of fog water droplets towards the surface, which
620 results in liquid water deposition on the surface if deposition rate is greater than the evaporation
621 rate. Conversely, a negative sign of the total liquid water flux indicates a net flow of water droplets
622 away from the surface, which can result in liquid water removal from the surface.

623

624 Interestingly, for all three fog cases, we notice that the magnitude of the LWF_{total} reaches its
625 maximum for water droplets with larger sizes of 20–45 μm , as indicated by the background maps.
626 For the fog case of 27 January 2022 (Fig. 9a), we remark that LWF_{turb} is significantly larger
627 compared to the magnitude of LWF_{grav} . This indicates that the fog deposition is mainly dominated
628 by the turbulent component and that the gravitational sedimentation process plays a lesser role in
629 this case. The turbulent part is larger than the settling component by a factor of 2.35. This can be
630 explained by the fact that the atmospheric turbulence during the fog event of 27 Jan. 2022 is well
631 developed (see Fig. 8b) and, as a result, large fog droplets with greater mass and momentum are
632 easily entrained by turbulent eddies and are more likely to collide or deposit onto the surface
633 through the turbulent flow. The cumulative sum of the total liquid water flux converted to
634 millimeters leads to the value of -0.18 mm as a net gain for the surface. Conversely, we notice that
635 the fog deposition due to the gravitational sedimentation mechanism prevails over the turbulent
636 process for both fog events observed on 04 and 24 February 2022. The gravitational settling
637 component is larger than the turbulent part by a factor of 7 for 04 February 2022, and by a factor
638 of 1.75 for 24 February 2022 fog case. The time-integrated total liquid water flux over the duration
639 of each fog event converted to millimeters leads to the values of -0.34 mm and -0.19 mm as net
640 gain for the surface respectively for 04 and 24 February 2022 fog events. It should be mentioned
641 that the values of the net flux of deposited water for these three fog events are close to those
642 reported by Spirig et al. (2021) in their study aimed at investigating the seasonality of fog over the
643 central arid Namib desert.

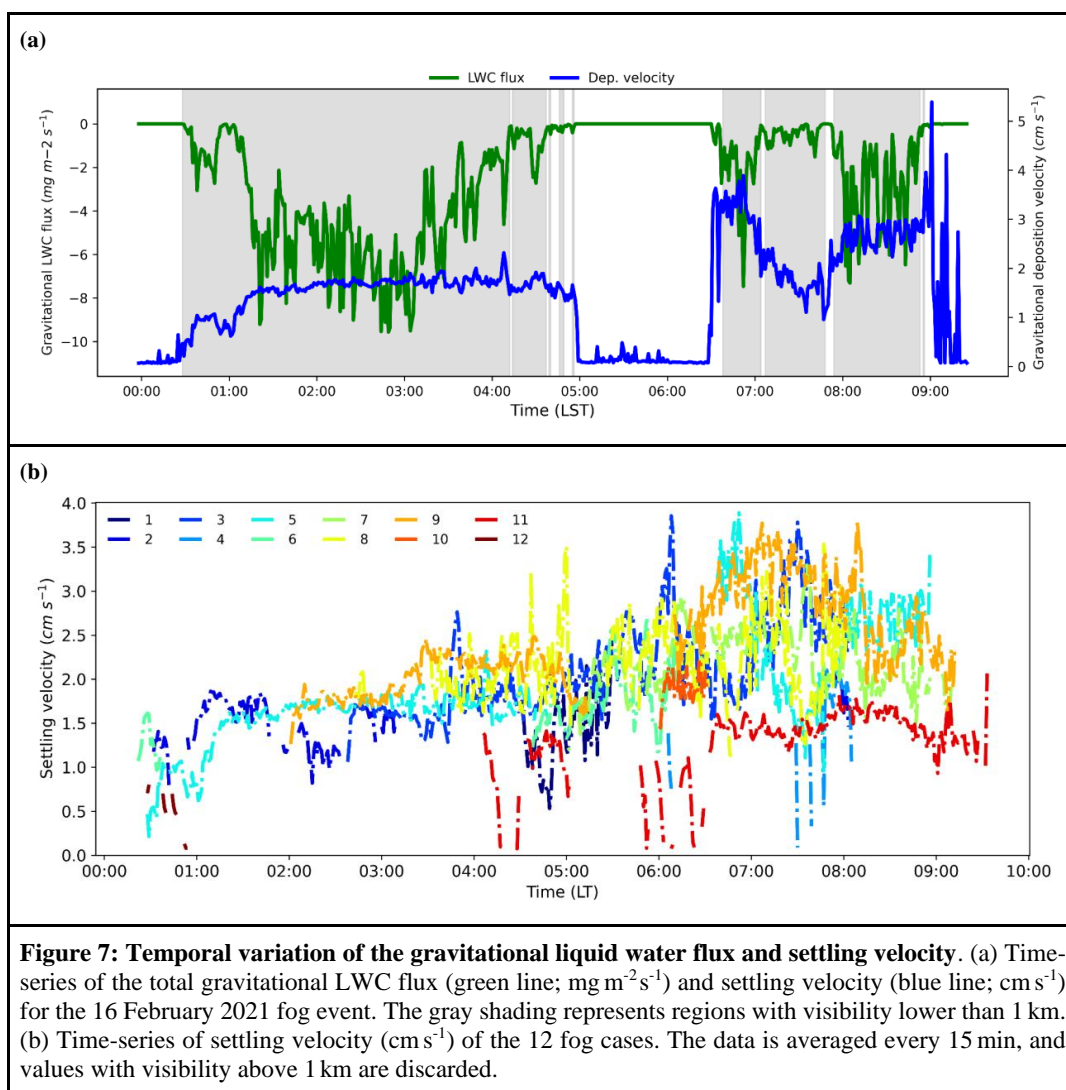
644

645 In this section, we calculated fog deposition velocities and net fluxes of liquid water deposited at
646 the surface for three fog events measured at the Barakah site using the EC framework. The values
647 obtained are of the same order of magnitude as what has been reported in other studies using the



648 same technique for example as in Spirig et al. (2021), Gultepe and Milbrandt (2007); Westbeld et
 649 al. (2009); Weston et al. (2022), and in Kowalski and Vong (1999). However, it should be noted
 650 that the eddy covariance method may not be reliable in cases where the turbulence regime is not
 651 sufficiently well-developed. Thus, direct measurements of fog water deposition through the setup
 652 of a field experiment at Barakah is vital not only to validate the EC technique but also to obtain
 653 accurate estimates of fog deposition processes at the nuclear site.

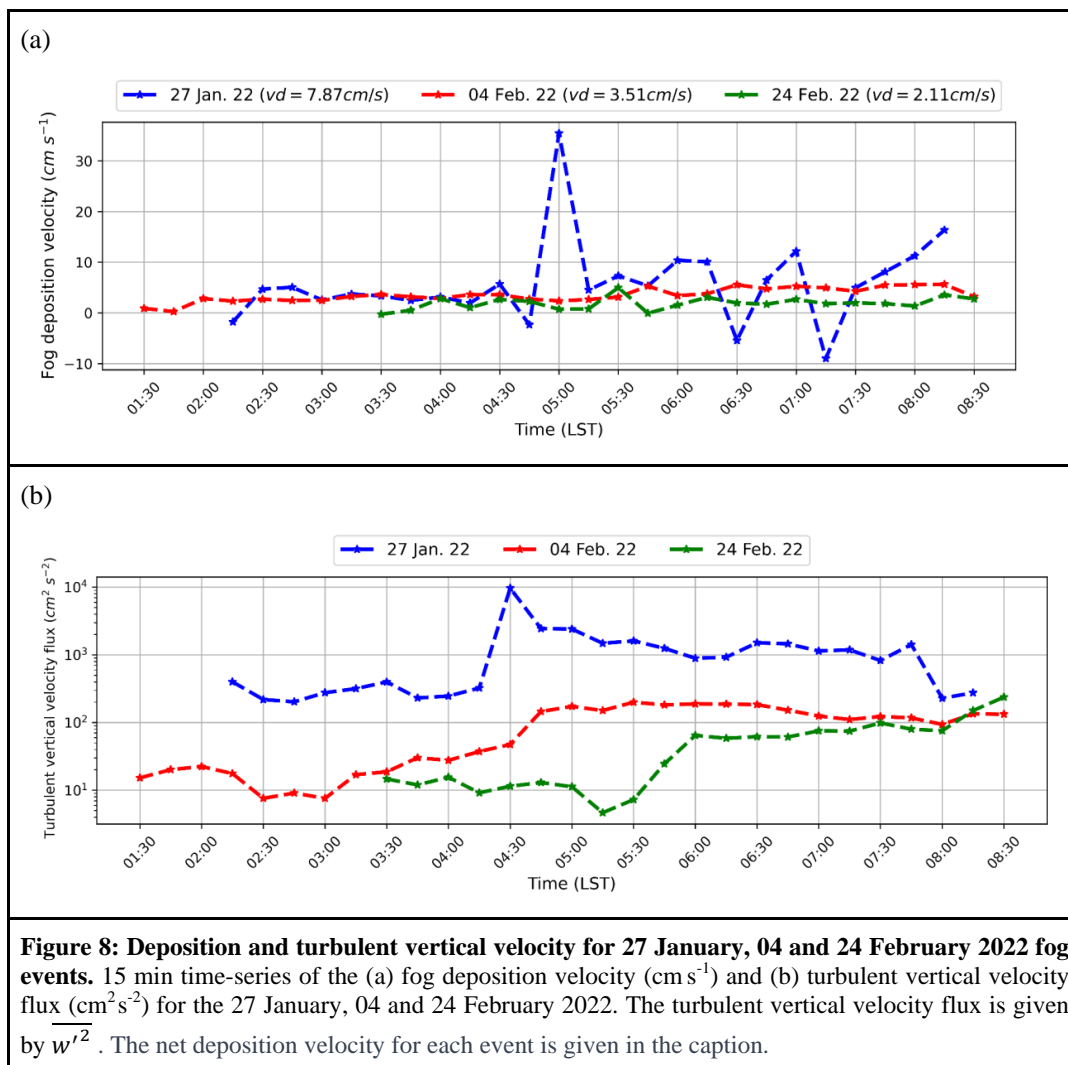
654
 655
 656



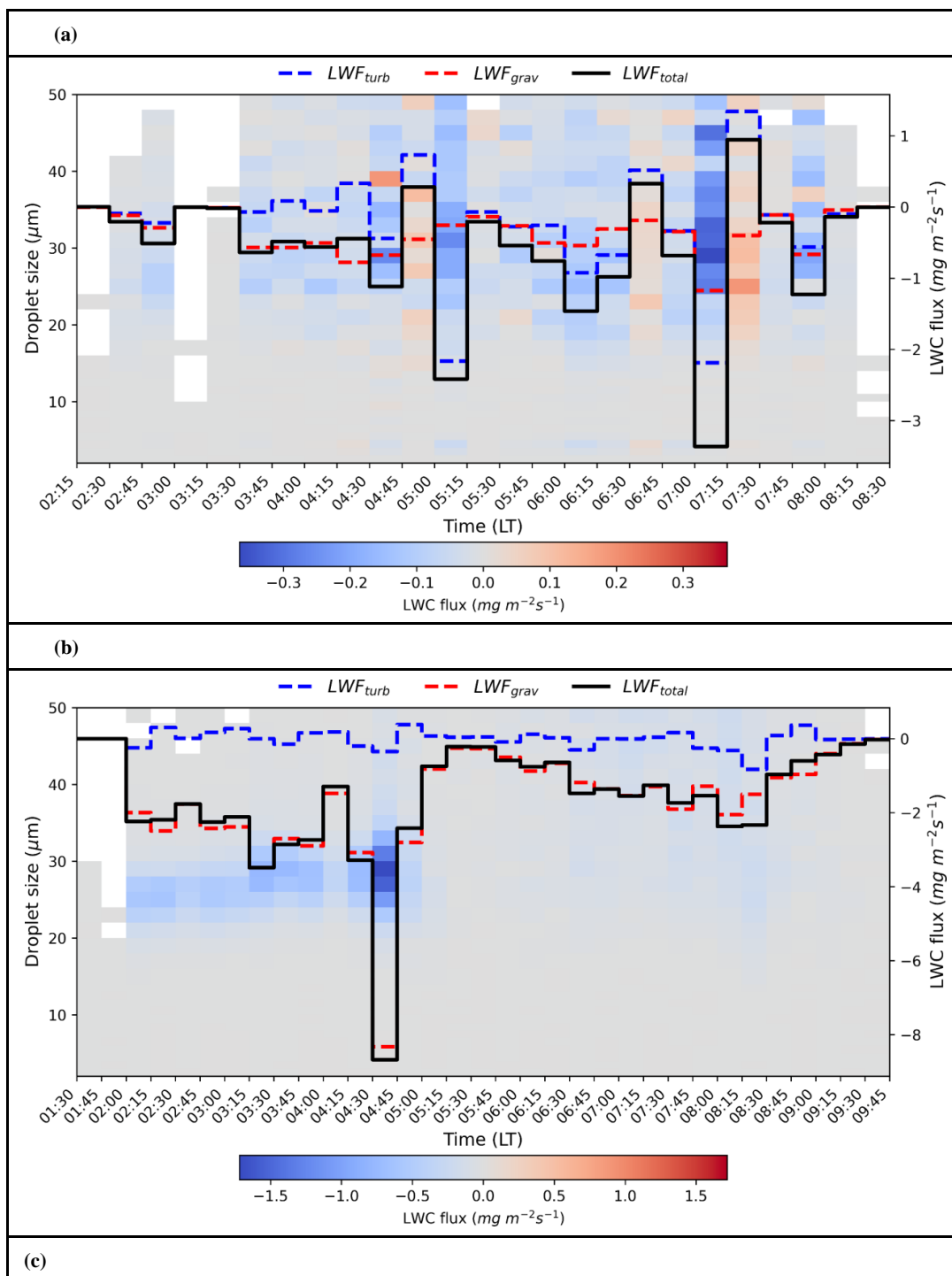
657
 658



659



660
661
662
663
664
665
666
667
668



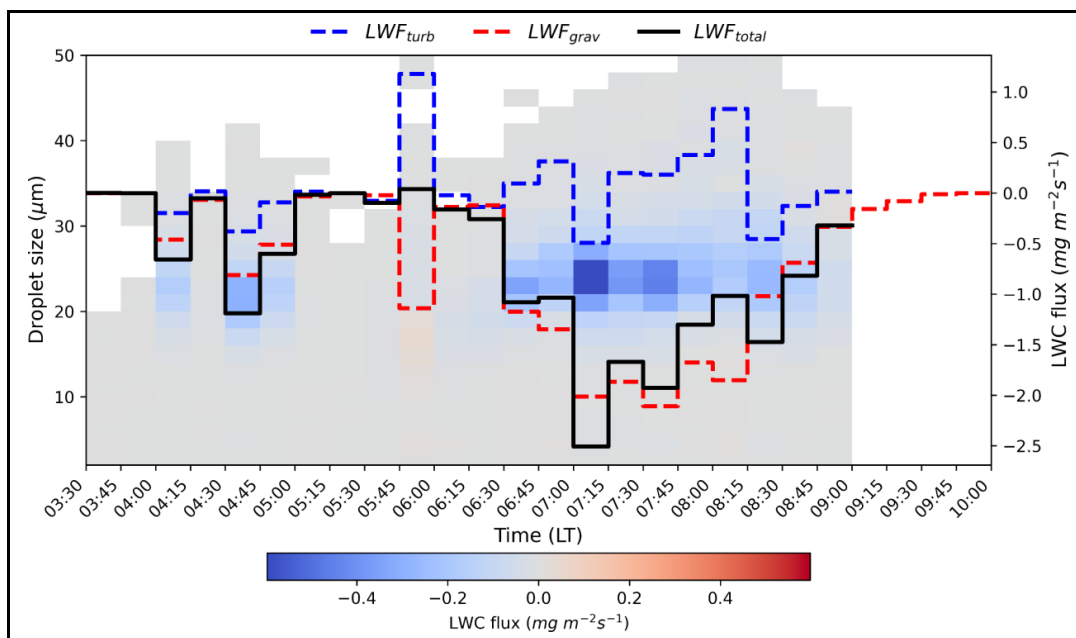


Figure 9: Liquid water flux for 27 January, 04 and 24 February 2022 fog events. 15-min liquid water flux ($\text{mg m}^{-2}\text{s}^{-1}$) components calculated for the three fog cases (a) 27 January, (b) 04 and (c) 24 February 2022. The turbulent liquid water flux, LWF_{turb} , is depicted in blue; the gravitational settling liquid water flux, LWF_{grav} , is depicted in red; the total liquid water flux, LWF_{total} , is depicted in black. The shading shows the temporal distribution of the total liquid water flux per bin droplet size. Note that EC data for the 24 February 2022 fog event was not available for the entire duration of the fog.

669

670

Table 4: Distribution of deposition settling velocities for different LWC bins.

LWC (mg m^{-3})	min (cm s^{-1})	max (cm s^{-1})	mean (cm s^{-1})	std (cm s^{-1})	count
000-100	0.08	3.77	1.95	0.65	1586
100-200	0.79	3.89	2.0	0.54	362
200-300	0.84	3.47	1.91	0.51	128
300-400	1.48	3.86	1.95	0.55	69
400-500	1.59	2.59	1.74	0.16	34
500-600	1.59	1.9	1.73	0.1	10



671

672

673 **5. Impact of fog on dispersion and deposition of radionuclides**

674 The goal of this section is to investigate the impact of fog on ground deposition of radioactive
675 materials in case of an accidental radioactive release at Barakah Nuclear Power Plant (BNPP). To
676 this end, we first use the Weather Research and Forecasting Model (WRF) to carry out a 3D non-
677 hydrostatic numerical simulation for a two-day period covering the fog event of 16th Feb. 2021.
678 Then, the generated WRF-forcing data are used to drive a state-of-the-art Atmospheric Transport
679 and Dispersion Model (ATDM) to simulate atmospheric radionuclide dispersion from a
680 hypothetical accidental radioactive release at BNPP.

681

682 Fog simulation is sensitive to the choice of the PBL parameterization scheme. Therefore, we
683 performed five 48-hour WRF simulations, using three local PBL schemes, MYJ, MYNN2.5 and
684 MYNN3.0, and two non-local PBL schemes. The model is initialized at 00 00 UTC on 15th Feb.
685 2021. The first twelve hours are discarded as spin-up time and the model output data were recorded
686 every 15 minutes. The innermost nested domain, which represents the study area, is illustrated in
687 Fig. 1b. These five model experiments would help evaluate the overall model's performance for
688 simulating the specific fog event observed on 16 Feb. 2021. Selecting the right PBL scheme is
689 essential to ensure accurate fog simulation results but at the same time it is a very difficult task in
690 modeling. However, it should be noted that the sensitivity test carried out in this study may provide
691 insights into the sensitivity of the model to various parameters related to the planetary boundary
692 layer. Having said that, it does not aim to provide a comprehensive assessment of the model's
693 performance for simulating fog over this hyper-arid region.

694

695 In the context of fog, the LWC is an important parameter for understanding the formation,
696 maintenance, and dissipation of fog. Fig. 10 shows a qualitative comparison between simulated
697 LWC by WRF and SEVIRI Fog RGB map for the fog event recorded on 16 February 2021 at
698 00:30 UTC. Figs. 10b and 10c depict the spatial patterns of the simulated LWC obtained by
699 averaging over the three lowest model levels (0-60m) for the nonlocal, ACM2, and the local, MYJ
700 PBL schemes, respectively. The SEVIRI RGB map (Fig. 10a) shows a band of fog along the entire
701 coastal regions of the UAE with a large fog patch near BNPP. The simulated LWC highlights that
702 both the nonlocal and the local PBL schemes are able to provide reasonable spatial patterns in
703 comparison with the SEVIRI RGB map. Besides, the nonlocal PBL scheme shows higher values
704 of LWC particularly near to the nuclear site and wider fog extent than the local PBL scheme. This
705 finding is in perfect agreement with Chen et al. (2020) results.

706

707 Figure 11a presents the modeled LWC from the first three model levels (0-60m) with the different
708 PBL schemes, along with the observed LWC for the fog case on 16 February, 2021. Figure 11b,
709 shows the diagnosed model visibility for the different PBL schemes using a power law relationship



710 that links the visibility to LWC as follows: $Vis = \alpha \times LWC^\beta$. This relationship is fitted using
711 visibility and LWC observations for the twelve fog cases. The regression coefficients α, β have the
712 values 0.94641 and -0.31572, respectively (Fig. A5). The LWC and visibility observations indicate
713 that the fog started at 00:30 (LST). With the lower nighttime temperatures, the fog lasted for 4 hr
714 and 15 min until 4:45 am, burning off one hour before sunrise. It is noteworthy that even though
715 most of the fog had swiftly dissipated just after sunrise, there were still some fog patches that
716 remained until 9 am. They may have been transported by wind towards the site, where it was
717 captured by the fog droplet monitor and the visibility meter.

718

719 As shown in Fig. 11, and for this specific fog event, we notice that the different PBL schemes used
720 in the model simulation have varying levels of accuracy in simulating the correct onset and
721 dissipation times of fog, especially between local and nonlocal schemes. Furthermore, we observe
722 that the simulated LWC in all the numerical experiments has higher values than the observations.
723 Especially for nonlocal schemes (ACM2, YSU), where the modeled LWC values are almost twice
724 as high. This result was also pointed out by Chen et al. (2020) and Ghude et al. (2023). Except for
725 the nonlocal ACM2 scheme, all other PBL schemes were able to simulate the fog onset time almost
726 exactly. However, they failed to capture the correct fog dissipation time as they showed earlier
727 dissipation times than those observed (with an average of 2 hours). In contrast, the nonlocal ACM2
728 scheme simulated the fog onset time 1 h late and appears to capture the fog dissipation time
729 reasonably well. Remarkably, we note that the local MYJ scheme succeeded in capturing the
730 remnant of the fog while all other PBL schemes have failed.

731

732 Here, we use meteorological output data from the WRF-MYJ model experiment to drive
733 FLEXPART in forward mode to simulate the transport and deposition of radionuclides at high-
734 spatial resolution (1 km) due to a hypothetical accidental radioactive release occurring at BNPP.
735 A radioactive release of ^{137}Cs as aerosol isotope with an emission rate of 10^{14} Bq h⁻¹ over a 28-
736 hour duration is considered. ^{137}Cs has a large radiological soil contamination impact due to its long
737 half-life (~ 30 years).

738

739 In order to highlight the impact of the fog deposition process on the ground deposition of
740 radionuclides, we perform two dispersion simulations for the case of the fog of 16 February, 2021.
741 The first simulation is run with the default parameters of the dispersion model, while the second
742 is run with the modification made to the gravitational sedimentation scheme as described earlier.
743 In both, FLEXPART is integrated over 48 hours from 00:00 UTC on 15 February, 2021, and the
744 radioactive release is assumed to start 20 hours after initialization. The dispersion model output
745 data is recorded every 15 minutes. Figures 12a-b show the spatial distribution of the total
746 deposition of ^{137}Cs to the ground (sum of dry and wet deposition) integrated from 08:15 to 08:30
747 LT on 16 February, 2021, respectively from the baseline simulation and that carried out under
748 foggy conditions. As expected, we observe a noticeable downwind increase in ground deposition
749 caused by the fog deposition process, which will subsequently lead to higher levels of soil



750 contamination. To gain more insight into how the fog occurrence impacts the temporal variation
751 of the ground deposition, we computed the time-variation of the contaminated land areas of ^{137}Cs
752 for a level value of 200 Bq m^{-2} . The contaminated area is calculated by counting the number of
753 land grid cells in the model domain for which combined values of dry and wet deposition are
754 greater than 200 Bq m^{-2} . Each model grid cell has an area of 1 km^2 . Figure 12c shows the temporal
755 variation of the contaminated areas for both the reference dispersion simulation and that with the
756 effect of fog deposition included. We notice that the contaminated land areas of the two dispersion
757 simulations show similar temporal variation patterns, and a gradual increase to reach their first
758 peaks around 10:00 LT, a few hours after the accidental release. Besides, the contaminated land
759 areas calculated under foggy conditions show higher values than those of the baseline simulation,
760 particularly from 00:00 to 12:00 LT where the fog event was measured at BNPP. It should be noted
761 that after the complete dissipation of the fog around 9:00 a.m. LT, the values of the contaminated
762 land region considering the fog deposition begin to gradually decrease to have values similar to
763 those of the reference simulation. In addition, to quantify the relative contribution of the fog
764 deposition process to the total ground deposition (dry and wet deposition combined) of ^{137}Cs , we
765 first integrated in time the two dispersion simulations over 28 hours after the start of the radioactive
766 release. Then, we calculated the ratio of the deposition field under foggy conditions to that of the
767 simulation of reference. Figure 12d shows the spatial distribution of this ratio given in percentage.
768 Remarkably, we observe that the fog deposition contributed to the total ground deposition by 30-
769 40%, and regions with marked increases in ground deposition are located near to the source. In
770 addition, it should be noted that the effect of the fog deposition is relatively small near the edges
771 of the radioactive plume where strong gradients exist.

772

773 In this section we have performed a simple modeling simulation experiment to highlight the
774 potential impact of fog on radionuclide ground deposition. It has been demonstrated in this test
775 case that the fog deposition enhances the deposition of ^{137}Cs radionuclide on the ground by acting
776 as a scavenging agent. The actual impact of fog on radionuclide deposition can vary widely
777 depending on the specific situation. Moreover, the solubility and chemical form of the
778 radionuclide-labeled particles can significantly influence this impact. For example, in cases where
779 the radionuclides are highly volatile or have a short half-life, fog may not have a significant effect
780 on their deposition. In other cases, the wind direction and speed can also play a role, as they can
781 affect how the fog and radionuclides are dispersed and transported. Yet, further modeling efforts
782 are needed to incorporate an accurate fog deposition scheme into the WRF model or into the
783 dispersion atmospheric model fitted to the BNPP region.

784

785

786

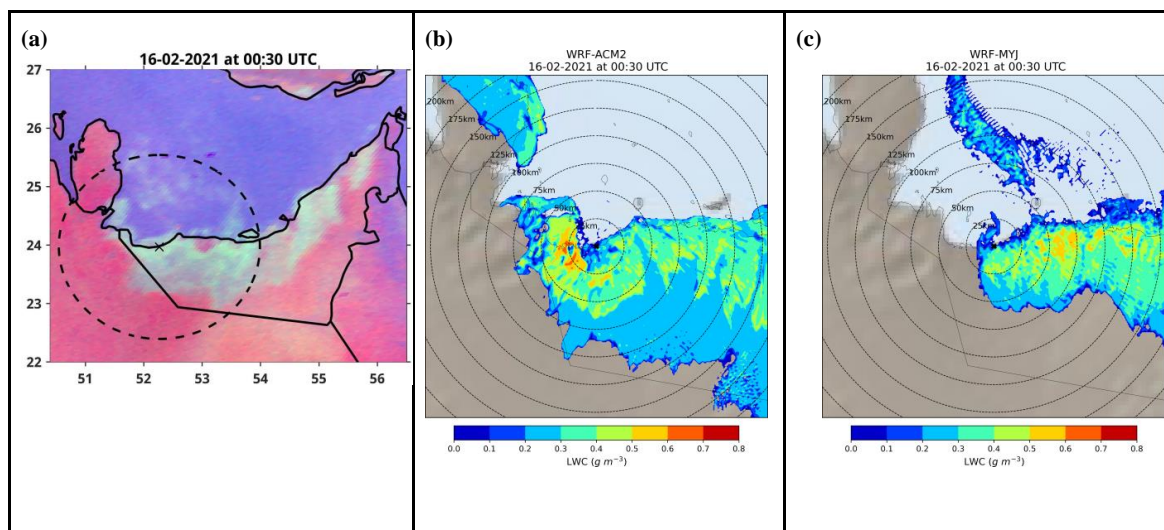
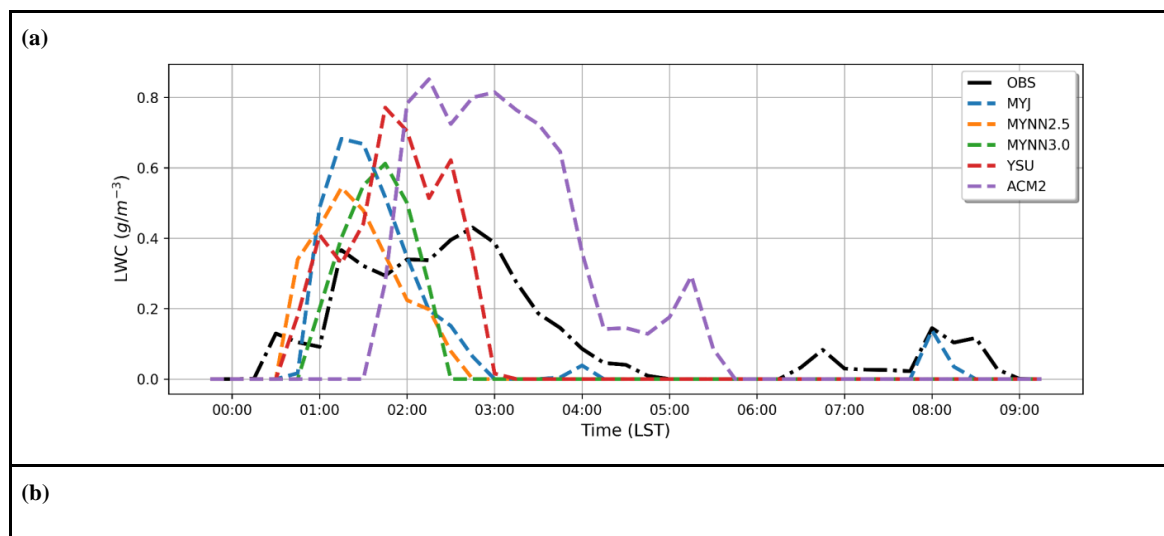


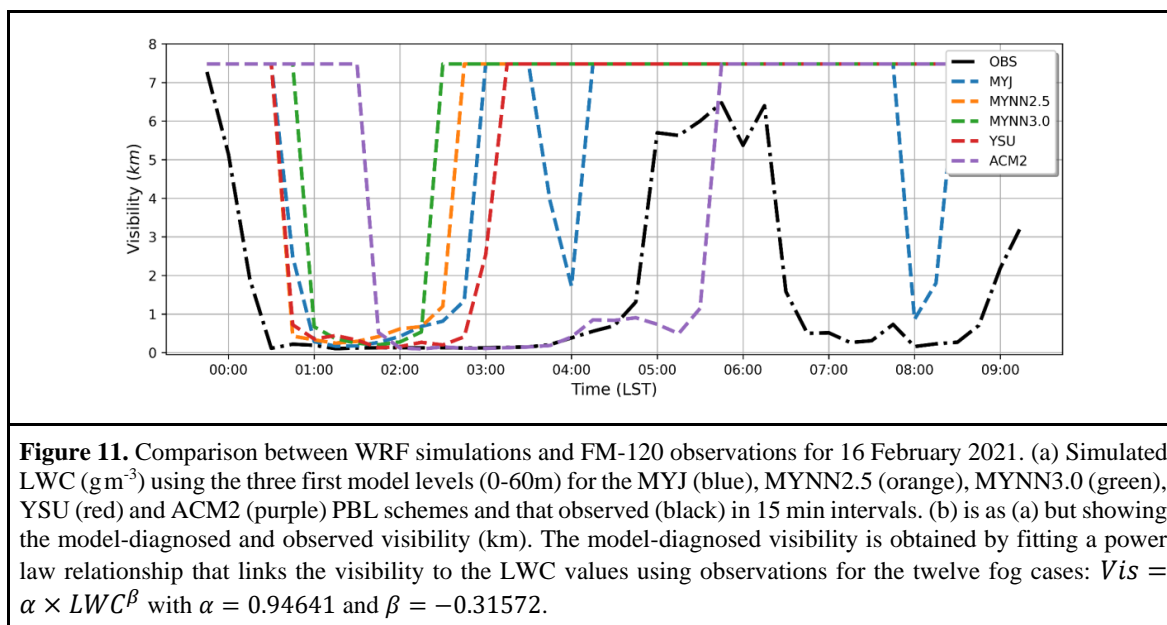
Figure 10. Comparison between WRF simulation and SEVIRI Fog RGB on 16 February 2021 at 00:30 UTC. (a) SEVIRI Fog RGB map. The dashed circle has a radius of 200 km and is centered at Barakah. (b) and (c) show the WRF simulated spatial pattern of LWC averaged over the three lowest model levels (0-60 m) using respectively the nonlocal (ACM2) and local (MYJ) PBL schemes.

787

788

789





790
791
792
793
794
795
796
797



798

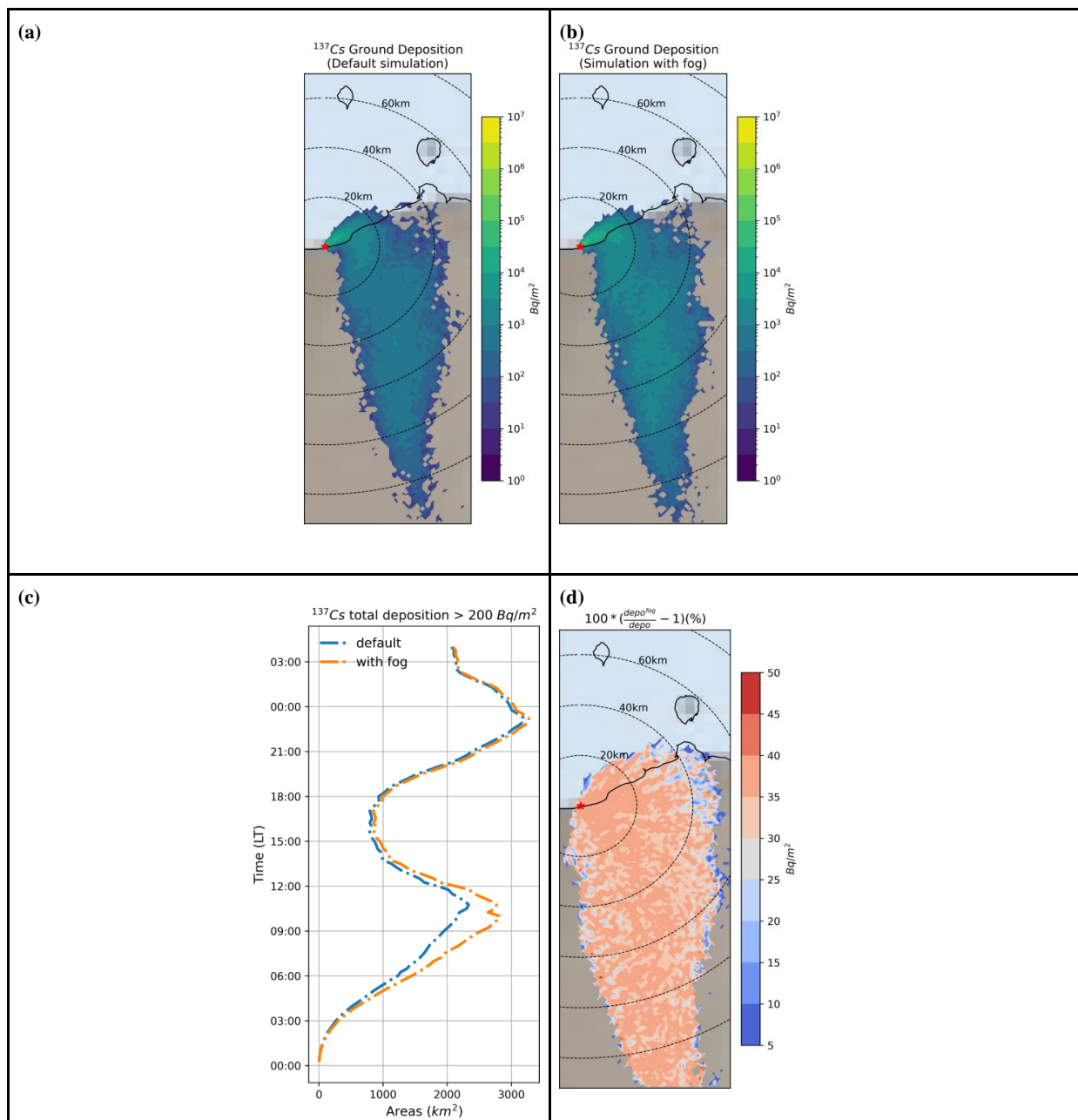


Figure 12: Quantification of the effect of fog deposition on the total radionuclide's deposition (combined dry and wet). (a) and (b) spatial distribution of the total surface deposition of ^{137}Cs integrated from 08:15 to 08:30 LT on 16 February 2021, respectively for the baseline simulation and that carried out under foggy conditions. (c) Temporal variation of the contaminated land area for the level 200 Bq/m^2 . The contaminated area is calculated by counting the number of land grid cells in the model domain for which combined values of dry and wet deposition are greater than 200 Bq/m^2 . Each model grid cell has an area of 1 km^2 . (d) Fractional contribution (%) of fog deposition to the total surface deposition of ^{137}Cs .



799 6. Conclusions

800 The main objective of this paper was to characterize the deposition of fog droplets around the
801 Barakah nuclear site and to perform a modeling simulation experiment to explore the impact of
802 fog deposition on the ground deposition of radionuclides in the event of a radiological emergency
803 at the site leading to the release of radioactive materials into the air.

804 State-of-the-art in-situ instruments including a ground-based radiometer, fog monitor sampler,
805 ultrasonic anemometer, and visibility meter have been deployed around the site to probe fog events
806 during the winter seasons of 2021 and 2022, and twelve cases of fog were recorded. The
807 microphysical properties for each fog event were inferred by analyzing data of horizontal visibility,
808 liquid water content (LWC), number concentrations (N_c), and median volume diameter data
809 (MVD). Analysis of the size distribution of the mean number concentration for each fog event
810 revealed that all observed fogs exhibit the same bimodal distribution shape, with modes at 4.5 and
811 23.2 μm , indicating the coexistence of two distinct populations of droplets in the fog, with a high
812 proportion of small droplets compared to the number of large droplets. The size distribution of the
813 mean LWC showed also a bimodal distribution with a broadening peak at 5.5 μm and a pronounced
814 peak at 25 μm . This confirmed that the greatest contribution to the LWC originates mainly from
815 large droplets, between 15 and 35 μm , despite their lower number concentration. The time-varying
816 number and mass densities revealed that at the onset stage, the smaller to medium-sized droplets
817 (1-10 μm) formed by condensation of water vapor contribute more to the LWC and account for up
818 to 85% of the total number of droplets. However, the large droplets (10-50 μm) formed mainly by
819 the collision-coalescence process at the mature stage, representing less than 20% of the total
820 number of droplets. They account for up to 90% of the total condensed water. Moreover, the MVD
821 ranges from 20 to 26 μm in almost all cases, suggesting that the radiation fogs observed in this
822 region tend to form larger droplets.

823

824 The microphysical mechanisms of condensation, coalescence, and evaporation impact the
825 number density and size distribution of water droplets in the fog, which in turn affect the rate of
826 fog droplet deposition on the surface. This study is the first application of the Eddy Covariance
827 (EC) framework to measure the fog droplet deposition velocity to a hyper arid coastal site. The EC
828 technique was applied for three fog events recorded at the Barakah site on January 27, 2022,
829 February 4, 2022 and February 24, 2022. The LWC flux in the fog is calculated as the sum of the
830 turbulent and gravitational settling components. As expected, higher amplitudes of liquid water
831 flux are found to be attributed more to larger-size droplets. For the fog case of January 27, 2022,
832 the fog deposition is found to be primarily controlled by turbulence, with a net gain deposited
833 water for the surface of about -0.18 mm, and an average deposition velocity of 7.9 cm s^{-1} .
834 Conversely, the fog deposition was found to be largely attributed to the gravitational sedimentation
835 process for the fog events of February 4, 2022, and February 24, 2022, with net gains for the
836 surface of about -0.34 mm, and -0.19 mm, and average deposition velocities of about 3.5 cm s^{-1} ,
837 and 2.1 cm s^{-1} respectively.

838

839 The calculated net fluxes of water deposited on the surface are found to be of the same order of
840 magnitude as what has been reported in some studies using the same technique (e.g., Kowalski and



841 Vong, 1999; Spirig et al., 2021, Gultepe and Milbrandt, 2007; Westbeld et al., 2009 and Weston
842 et al., 2022). Moreover, the typical values of the average fog deposition rate calculated for these
843 three fog events are of a similar magnitude to the values reported by Tav et al., (2018) for the bare
844 surface type. However, it should be noted that the EC method may not be reliable in cases where
845 the turbulence regime is not sufficiently well-developed.

846

847 In order to assess the impact of fog deposition on ground deposition of radionuclides released
848 into the air in case of an accidental radioactive release occurring at BNPP, a modeling simulation
849 experiment was carried out. The ratio of the time-integrated ground deposition of ^{137}Cs under
850 foggy conditions to that of the baseline simulation, showed that the fog deposition contributed to
851 the total ground deposition of ^{137}Cs by 30 to 40%. This result demonstrated that incorporating the
852 fog deposition process in dispersion modeling as an additional scavenging mechanism is vital
853 under foggy conditions. This is consistent with previous findings; in France for instance and based
854 on model simulations, it has been found that the presence of a fog during a nuclear accident could
855 lead to an almost twice higher surface contamination density of ^{137}Cs than without fog and with
856 only dry deposition (e.g., Masson et al., 2015).

857

858 Our findings are useful for future work on fog deposition and field campaigns in this semi-arid
859 region. The study will be extended by applying the Eddy Covariance technique to estimate the fog-
860 droplet deposition rates to additional fog events. It would be enlightening to plan a field experiment
861 to acquire direct measurements of fog deposition at the site by a sensitive weighing method, and
862 collection of fog water for further analysis. This will help not only to validate the EC technique
863 but also to better estimate the fog deposition parameters. Also, this would help in evaluating the
864 performance of the fog deposition scheme in the WRF model. Additionally, further modeling
865 efforts are required to efficiently account for the fog deposition as an additional removal process
866 in dispersion modeling.

867

868 **Acknowledgment**

869 We would like to thank Khalifa University's high-performance computing and research computing
870 facilities for their support of this research work. This research work was supported by the Federal
871 Authority for Nuclear Regulation (FANR) through the research project Modeling of Radionuclides
872 Dispersion in the UAE Environment (MORAD). Nawah and SHAMS power companies are both
873 acknowledged for facilitating the deployment of instruments and conducting the field campaign in
874 the UAE desert.

875

876

877 **Conflict of Interest**

878 The authors declare they have no conflict of interest.

879

880 **Appendix**

881



882

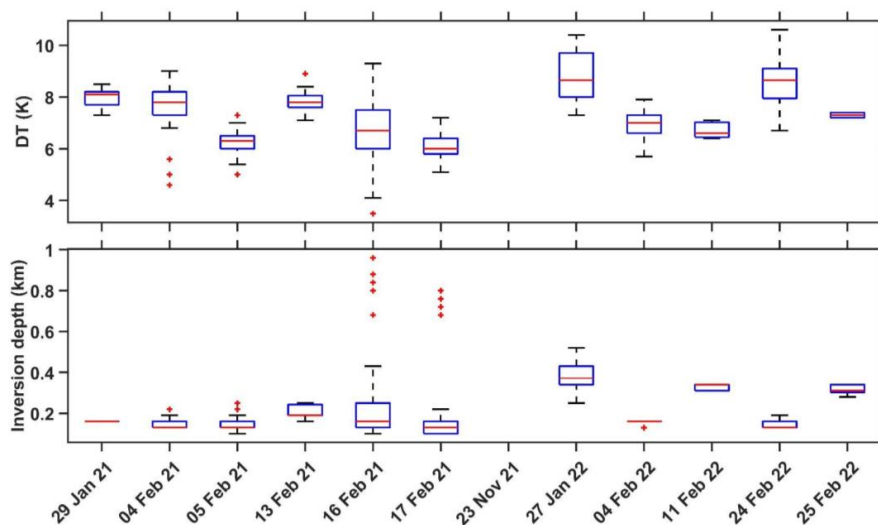
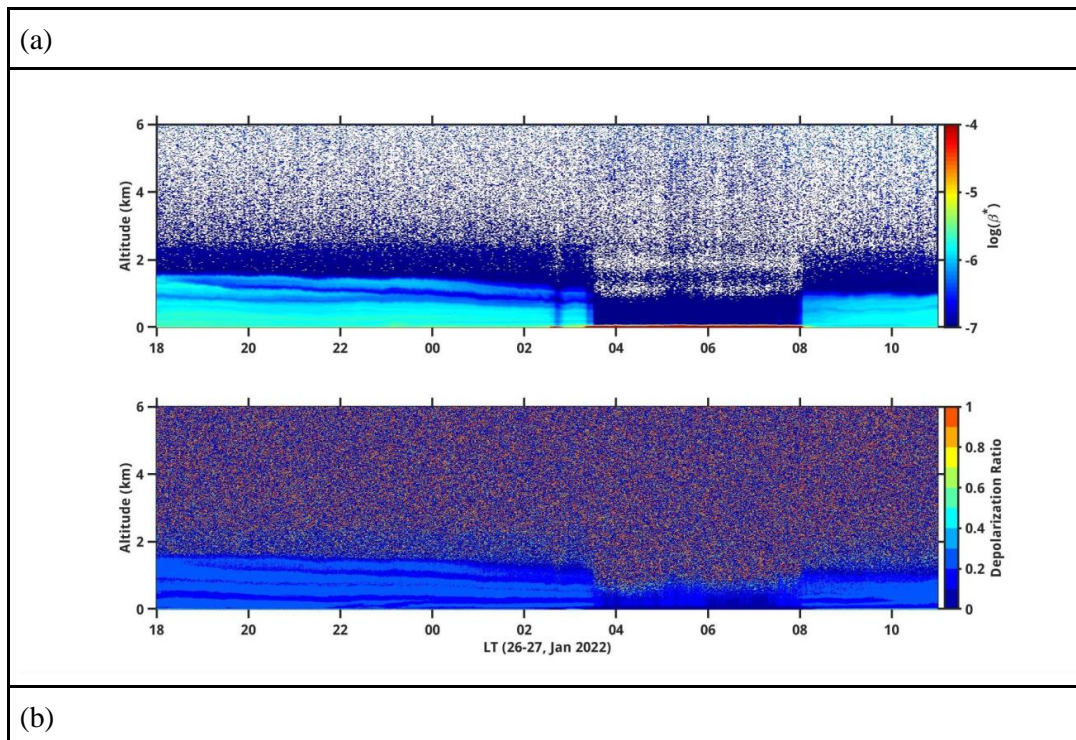


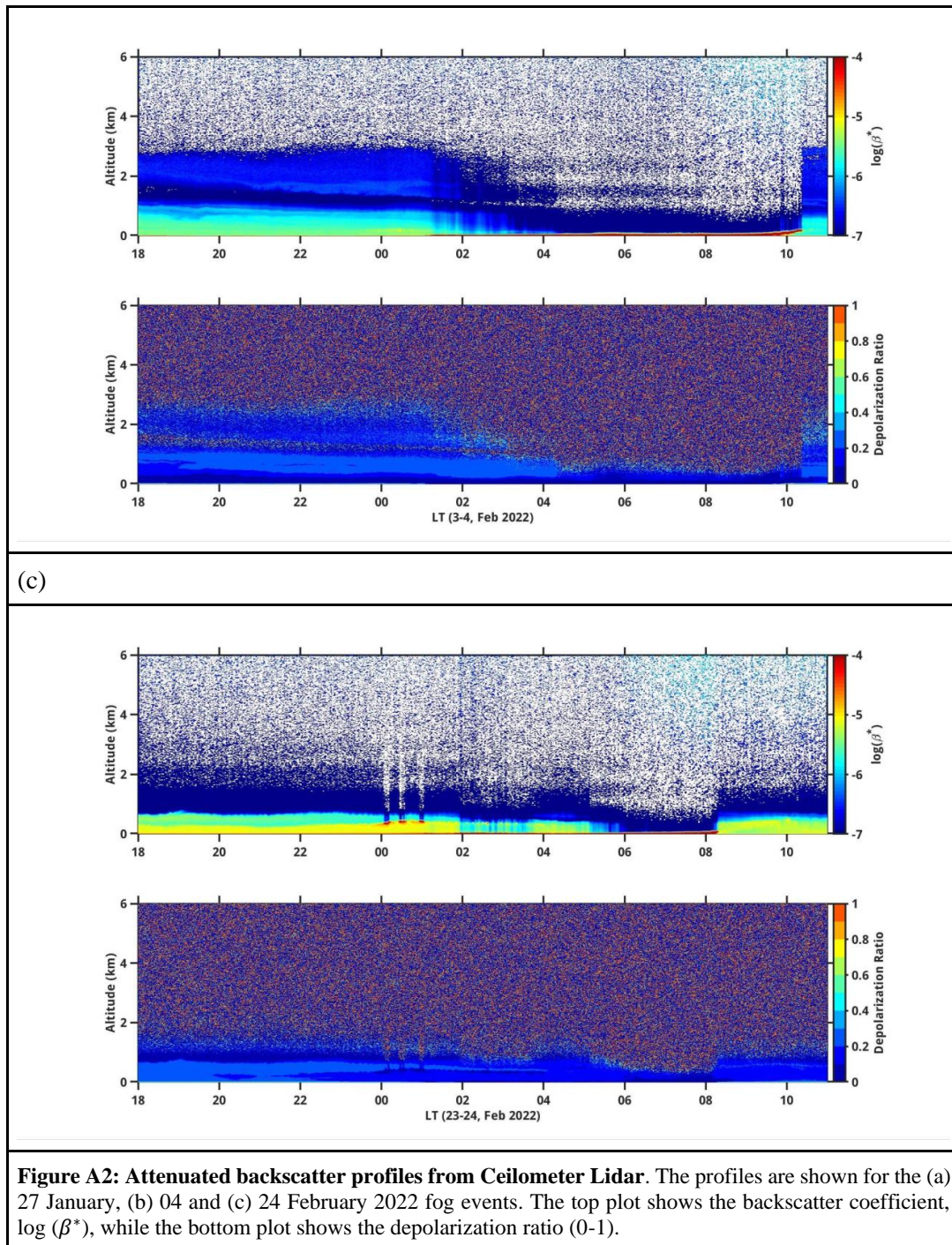
Figure A1: Temperature inversion during 12 fog events. Surface-based temperature inversion strength (top; K) and depth of the inversion layer (bottom; km) for the 12 fog events.

883

884

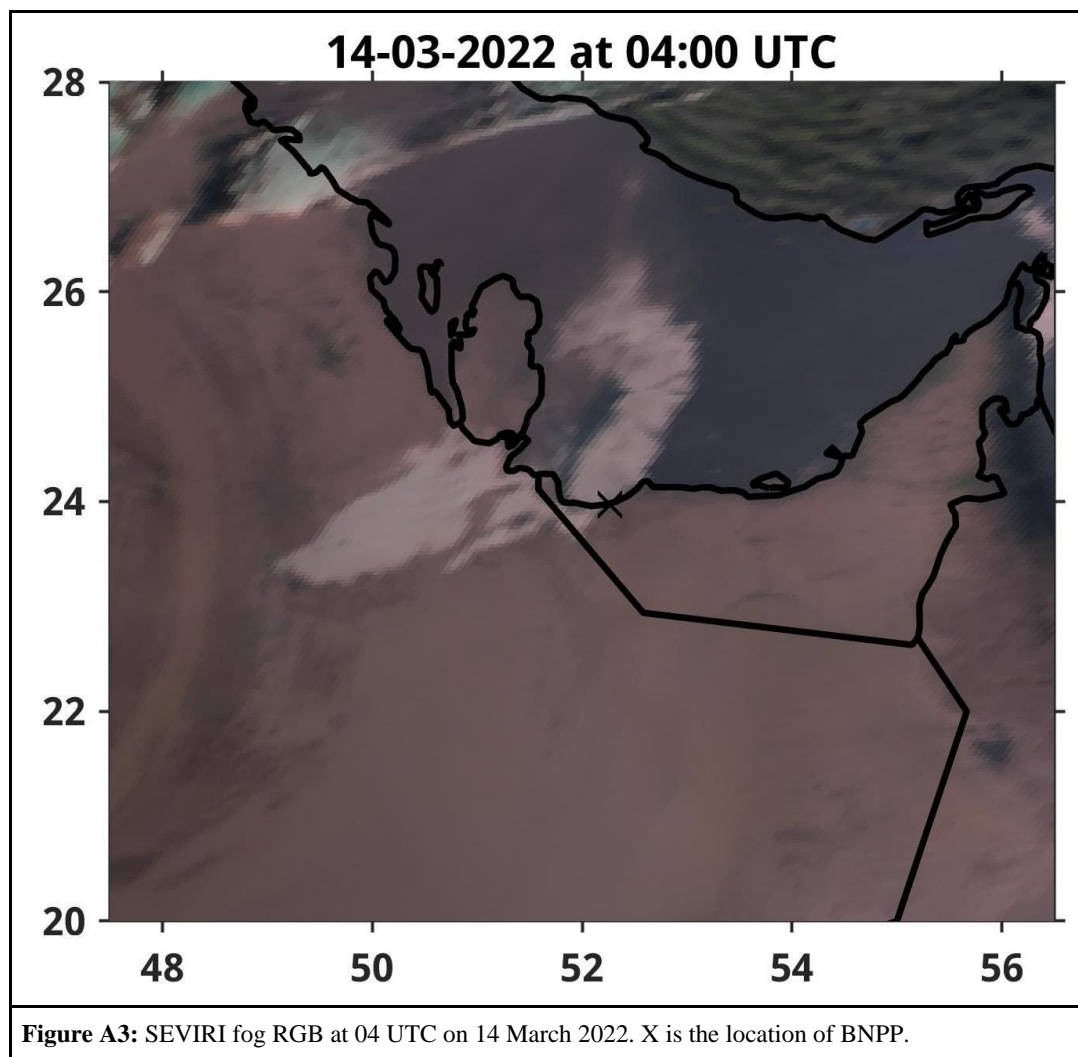
885





886

887



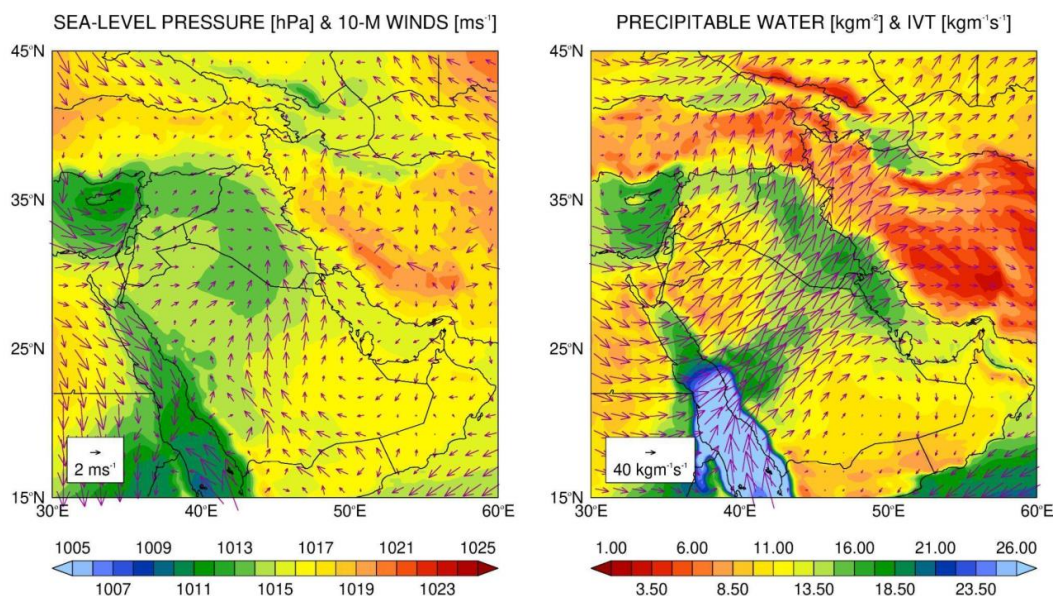
888

889

(a) ERA-5 full fields



12 FOG CASES @ 00-04UTC



(b) ERA-5 anomalies

ANOMALIES FOR 12 FOG CASES @ 00-04UTC

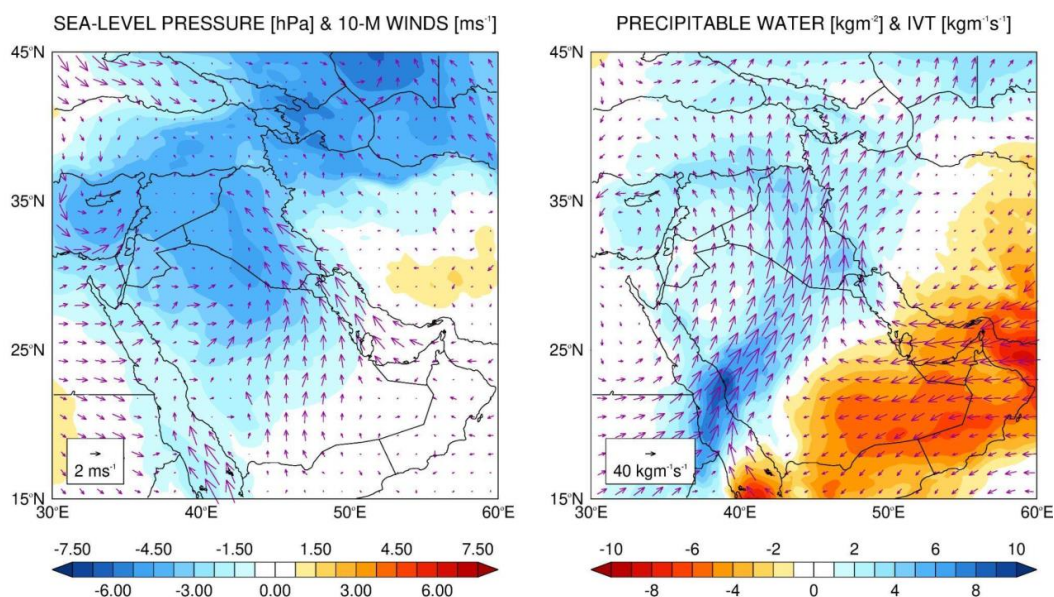
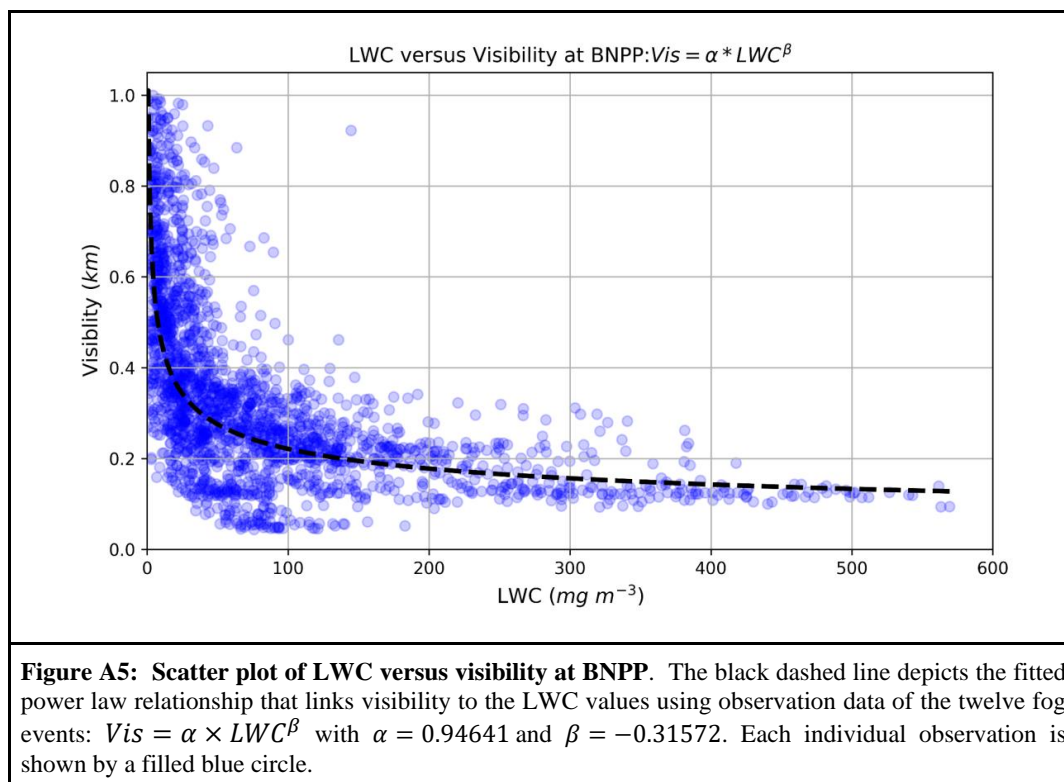


Figure A4: ERA-5 fields averaged over all 12 fog events. (a) Sea-level pressure (shading; hPa) and 10-m wind vectors (arrows; m s^{-1}) (left) and precipitable water (shading; kg m^{-2}) and integrated vapour transport (arrows; $\text{kg m}^{-1} \text{s}^{-1}$) (right) averaged over 00-04 UTC of the 12 fog days listed in Table S1. (b) is as (a) but showing anomalies with respect to ERA-5's 1979-2021 monthly climatology at the respective hour of day.



890



891

892

893 References

894

895 Abida, R., Addad, Y., Francis, D., Temimi, M., Nelli, N., Fonseca, R., Nesterov, O. and Bosc, E.:
896 Evaluation of the Performance of the WRF Model in a Hyper-Arid Environment: A Sensitivity Study,
897 Atmosphere, 13(6), 985, <https://doi.org/10.3390/atmos13060985>, 2022.

898 Aldababseh, A. and Temimi, M.: Analysis of the Long-Term Variability of Poor Visibility Events in the
899 UAE and the Link with Climate Dynamics, Atmosphere, 8(12), 242,
900 <https://doi.org/10.3390/atmos8120242>, 2017.

901 Bahreini, R., Ervens, B., Middlebrook, A. M., Warneke, C., de Gouw, J. A., DeCarlo, P. F., Jimenez, J. L.,
902 Brock, C. A., Neuman, J. A., Ryerson, T. B., Stark, H., Atlas, E., Brioude, J., Fried, A., Holloway, J. S.,
903 Peischl, J., Richter, D., Walega, J., Weibring, P., Wollny, A. G. and Fehsenfeld, F. C.: Organic aerosol
904 formation in urban and industrial plumes near Houston and Dallas, Texas, J. Geophys. Res., 114,
905 <https://doi.org/10.1029/2008JD011493>, 2009.

906 Beswick, K. M., Hargreaves, K. J., Gallagher, M. W., Choularton, T. W. and Fowler, D.: Size-resolved
907 measurements of cloud droplet deposition velocity to a forest canopy using an eddy correlation technique,
908 Q.J Royal Met. Soc., 117(499), 623–645, <https://doi.org/10.1002/qj.49711749910>, 1991.



- 909 Boutle, I., Price, J., Kudzotsa, I., Kokkola, H. and Romakkaniemi, S.: Aerosol–fog interaction and the
910 transition to well-mixed radiation fog, *Atmospheric Chemistry and Physics*, 18(11), 7827–7840,
911 <https://doi.org/10.5194/acp-18-7827-2018>, 2018.
- 912 Brioude, J., Arnold, D., Stohl, A., Cassiani, M., Morton, D., Seibert, P., Angevine, W., Evan, S., Dingwell,
913 A., Fast, J. D., Easter, R. C., Pisso, I., Burkhardt, J. and Wotawa, G.: The Lagrangian particle dispersion
914 model FLEXPART-WRF version 3.1, *Geosci. Model Dev.*, 6(6), 1889–1904, <https://doi.org/10.5194/gmd-6-1889-2013>, 2013.
- 916 Cermak, J. and Bendix, J.: Dynamical nighttime fog/low stratus detection based on meteosat SEVIRI data:
917 A feasibility study, *Pure appl. geophys.*, 164(6–7), 1179–1192, <https://doi.org/10.1007/s00024-007-0213-8>, 2007.
- 919 Chaouch, N., Temimi, M., Weston, M. and Ghedira, H.: Sensitivity of the meteorological model WRF-
920 ARW to planetary boundary layer schemes during fog conditions in a coastal arid region, *Atmos. Res.*, 187,
921 106–127, <https://doi.org/10.1016/j.atmosres.2016.12.009>, 2017.
- 922 Chen, C., Zhang, M., Perrie, W., Chang, R., Chen, X., Duplessis, P. and Wheeler, M.: Boundary layer
923 parameterizations to simulate fog over atlantic canada waters, *Earth and Space Science*, 7(3),
924 <https://doi.org/10.1029/2019EA000703>, 2020.
- 925 Cooper, O. R., Parrish, D. D., Stohl, A., Trainer, M., Nédélec, P., Thouret, V., Cammas, J. P., Oltmans, S.
926 J., Johnson, B. J., Tarasick, D., Leblanc, T., McDermid, I. S., Jaffe, D., Gao, R., Stith, J., Ryerson, T., Aikin,
927 K., Campos, T., Weinheimer, A. and Avery, M. A.: Increasing springtime ozone mixing ratios in the free
928 troposphere over western North America., *Nature*, 463(7279), 344–348,
929 <https://doi.org/10.1038/nature08708>, 2010.
- 930 Degeffie, D. T., El-Madany, T. S., Hejkal, J., Held, M., Dupont, J. C., Haeffelin, M. and Klemm, O.:
931 Microphysics and energy and water fluxes of various fog types at SIRTa, France, *Atmos. Res.*, 151, 162–
932 175, <https://doi.org/10.1016/j.atmosres.2014.03.016>, 2015.
- 933 Eckardt, F. D. and Schemenauer, R. S.: Fog water chemistry in the Namib desert, Namibia, *Atmos.*
934 *Environ.*, 32(14–15), 2595–2599, [https://doi.org/10.1016/S1352-2310\(97\)00498-6](https://doi.org/10.1016/S1352-2310(97)00498-6), 1998.
- 935 Egli, S., Maier, F., Bendix, J. and Thies, B.: Vertical distribution of microphysical properties in radiation
936 fogs — A case study, *Atmos. Res.*, 151, 130–145, <https://doi.org/10.1016/j.atmosres.2014.05.027>, 2015.
- 937 Ellrod, G. P. and Gultepe, I.: Inferring low cloud base heights at night for aviation using satellite infrared
938 and surface temperature data, *Pure appl. geophys.*, 164(6–7), 1193–1205, <https://doi.org/10.1007/s00024-007-0214-7>, 2007.
- 940 Eugster, W., Burkard, R., Holwerda, F., Scatena, F. N. and Bruijnzeel, L. A. (Sampurno): Characteristics
941 of fog and fogwater fluxes in a Puerto Rican elfin cloud forest, *Agricultural and Forest Meteorology*, 139(3–
942 4), 288–306, <https://doi.org/10.1016/j.agrformet.2006.07.008>, 2006.
- 943 Feigenwinter, C., Franceschi, J., Larsen, J. A., Spirig, R. and Vogt, R.: On the performance of
944 microlysimeters to measure non-rainfall water input in a hyper-arid environment with focus on fog
945 contribution, *J. Arid Environ.*, 182, 104260, <https://doi.org/10.1016/j.jaridenv.2020.104260>, 2020.
- 946 Fonseca, R., Francis, D., Nelli, N. and Thota, M.: Climatology of the heat low and the intertropical
947 discontinuity in the Arabian Peninsula, *Int. J. Climatol.*, 42(2), 1092–1117,
948 <https://doi.org/10.1002/joc.7291>, 2022.
- 949 Fonseca, R., Francis, D., Nelli, N. and Cherif, C.: Regional atmospheric circulation patterns driving
950 consecutive fog events in the United Arab Emirates, *Atmos. Res.*, 282, 106506,
951 <https://doi.org/10.1016/j.atmosres.2022.106506>, 2023.



- 952 Formenti, P., D'Anna, B., Flamant, C., Mallet, M., Piketh, S. J., Schepanski, K., Waquet, F., Auriol, F.,
953 Brogniez, G., Burnet, F., Chaboureaud, J.-P., Chauvigné, A., Chazette, P., Denjean, C., Desboeufs, K.,
954 Doussin, J.-F., Elguindi, N., Feuerstein, S., Gaetani, M., Giorio, C. and Holben, B.: The Aerosols, Radiation
955 and Clouds in southern Africa (AEROCLO-sA) field campaign in Namibia: overview, illustrative
956 observations and way forward, *Bull. Amer. Meteor. Soc.*, <https://doi.org/10.1175/BAMS-D-17-0278.1>,
957 2019.
- 958 Francis, D., Chaboureaud, J.-P., Nelli, N., Cuesta, J., Alshamsi, N., Temimi, M., Pauluis, O. and Xue, L.:
959 Summertime dust storms over the Arabian Peninsula and impacts on radiation, circulation, cloud
960 development and rain, *Atmos. Res.*, 250, 105364, <https://doi.org/10.1016/j.atmosres.2020.105364>, 2021.
- 961 Francis, D., Fonseca, R., Nelli, N., Bozkurt, D., Cuesta, J. and Bosc, E.: On the Middle East's severe dust
962 storms in spring 2022: Triggers and impacts, *Atmos. Environ.*, 296, 119539,
963 <https://doi.org/10.1016/j.atmosenv.2022.119539>, 2023.
- 964 Gonser, S. G., Klemm, O., Griessbaum, F., Chang, S.-C., Chu, H.-S. and Hsia, Y.-J.: The relation between
965 humidity and liquid water content in fog: an experimental approach, *Pure appl. geophys.*, 169(5–6), 821–
966 833, <https://doi.org/10.1007/s00024-011-0270-x>, 2012.
- 967 Ghude, S. D., Jenamani, R. K., Kulkarni, R., Wagh, S., Dhangar, N. G., Parde, A. N., Acharja, P., Lonkar,
968 P., Govardhan, G., Yadav, P., Vispute, A., Debnath, S., Lal, D. M., Bisht, D. S., Jena, C., Pawar, P. V.,
969 Dhankhar, S. S., Sinha, V., Chate, D. M., Safai, P. D. and Rajeevan, M.: WiFEX: Walk into the warm fog
970 over Indo Gangetic Plain region, *Bull. Amer. Meteor. Soc.*, <https://doi.org/10.1175/BAMS-D-21-0197.1>,
971 2023.
- 972 Gultepe, I. and Milbrandt, J. A.: Microphysical Observations and Mesoscale Model Simulation of a Warm
973 Fog Case during FRAM Project, *Pure appl. geophys.*, 164(6–7), 1161–1178,
974 <https://doi.org/10.1007/s00024-007-0212-9>, 2007.
- 975 Gultepe, I., Pearson, G., Milbrandt, J. A., Hansen, B., Platnick, S., Taylor, P., Gordon, M., Oakley, J. P.
976 and Cober, S. G.: The fog remote sensing and modeling field project, *Bull. Amer. Meteor. Soc.*, 90(3), 341–
977 360, <https://doi.org/10.1175/2008BAMS2354.1>, 2009.
- 978 Gultepe, I., Milbrandt, J. A. and Zhou, B.: Marine fog: A review on microphysics and visibility prediction,
979 in *Marine fog: challenges and advancements in observations, modeling, and forecasting*, edited by D.
980 Koračin and C. E. Dorman, pp. 345–394, Springer International Publishing, Cham,
981 https://doi.org/10.1007/978-3-319-45229-6_7, , 2017.
- 982 Gultepe, I., Heymsfield, A. J., Fernando, H. J. S., Pardyjak, E., Dorman, C. E., Wang, Q., Creegan, E.,
983 Hoch, S. W., Flagg, D. D., Yamaguchi, R., Krishnamurthy, R., Gaberšek, S., Perrie, W., Perelet, A., Singh,
984 D. K., Chang, R., Nagare, B., Wagh, S. and Wang, S.: A Review of Coastal Fog Microphysics During C-
985 FOG, *Boundary Layer Meteorol.*, <https://doi.org/10.1007/s10546-021-00659-5>, 2021.
- 986 Hong, S.-Y., Noh, Y. and Dudhia, J.: A New Vertical Diffusion Package with an Explicit Treatment of
987 Entrainment Processes, *Mon. Wea. Rev.*, 134(9), 2318–2341, <https://doi.org/10.1175/MWR3199.1>, 2006.
- 988 Hososhima, M. and Kaneyasu, N.: Altitude-dependent distribution of ambient gamma dose rates in a
989 mountainous area of Japan caused by the Fukushima nuclear accident., *Environ. Sci. Technol.*, 49(6), 3341–
990 3348, <https://doi.org/10.1021/es504838w>, 2015.
- 991 Hůnová, I., Kurfuerst, P., Maznová, J. and Coňková, M.: The contribution of occult precipitation to sulphur
992 deposition in the Czech Republic, *Erdkunde*, 65(3), 247–259, <https://doi.org/10.3112/erdkunde.2011.03.03>,
993 2011.
- 994 Iacono, M. J., Delamere, J. S., Mlawer, E. J., Shephard, M. W., Clough, S. A. and Collins, W. D.: Radiative



- 995 forcing by long-lived greenhouse gases: Calculations with the AER radiative transfer models, *J. Geophys.*
996 *Res.*, 113(D13), <https://doi.org/10.1029/2008JD009944>, 2008.
- 997 Imamura, N., Katata, G., Kajino, M., Kobayashi, M., Itoh, Y. and Akama, A.: Fogwater deposition of
998 radiocesium in the forested mountains of East Japan during the Fukushima Daiichi Nuclear Power Plant
999 accident: A key process in regional radioactive contamination, *Atmos. Environ.*, 224, 117339,
1000 <https://doi.org/10.1016/j.atmosenv.2020.117339>, 2020.
- 1001 Janjić, Z. I.: The Step-Mountain Eta Coordinate Model: Further Developments of the Convection, Viscous
1002 Sublayer, and Turbulence Closure Schemes, *Mon. Wea. Rev.*, 122(5), 927–945,
1003 [https://doi.org/10.1175/1520-0493\(1994\)122<0927:TSMECM>2.0.CO;2](https://doi.org/10.1175/1520-0493(1994)122<0927:TSMECM>2.0.CO;2), 1994.
- 1004 Kain, J. S.: The kain–fritsch convective parameterization: an update, *J. Appl. Meteor.*, 43(1), 170–181,
1005 [https://doi.org/10.1175/1520-0450\(2004\)043<0170:TKCPAU>2.0.CO;2](https://doi.org/10.1175/1520-0450(2004)043<0170:TKCPAU>2.0.CO;2), 2004.
- 1006 Kaneyasu, N., Kutsuna, S., Iida, K., Sanada, Y. and Tajiri, T.: Cloudwater Deposition Process of
1007 Radionuclides Based on Water Droplets Retrieved from Pollen Sensor Data., *Environ. Sci. Technol.*,
1008 56(17), 12036–12044, <https://doi.org/10.1021/acs.est.2c02051>, 2022.
- 1009 Kaseke, K. F., Tian, C., Wang, L., Seely, M., Vogt, R., Wassenaar, T. and Mushi, R.: Fog Spatial
1010 Distributions over the Central Namib Desert - An Isotope Approach, *Aerosol Air Qual. Res.*, 18(1), 49–61,
1011 <https://doi.org/10.4209/aaqr.2017.01.0062>, 2018.
- 1012 Katata, G.: Fogwater deposition modeling for terrestrial ecosystems: A review of developments and
1013 measurements, *J. Geophys. Res. Atmos.*, 119(13), 8137–8159, <https://doi.org/10.1002/2014JD021669>,
1014 2014.
- 1015 Katata, G., Nagai, H., Kajino, M., Ueda, H. and Hozumi, Y.: Numerical study of fog deposition on
1016 vegetation for atmosphere–land interactions in semi-arid and arid regions, *Agricultural and Forest*
1017 *Meteorology*, 150(3), 340–353, <https://doi.org/10.1016/j.agrformet.2009.11.016>, 2010.
- 1018 Klemm, O. and Wrzesinsky, T.: Fog deposition fluxes of water and ions to a mountainous site in
1019 Central Europe, *Tellus B: Chemical and Physical Meteorology*, 59(4), 705, <https://doi.org/10.1111/j.1600-0889.2007.00287.x>, 2007.
- 1021 Kowalski, A. S. and Vong, R. J.: Near-surface fluxes of cloud water evolve vertically, *QJ Royal Met. Soc.*,
1022 125(559), 2663–2684, <https://doi.org/10.1002/qj.49712555916>, 1999.
- 1023 Lin, C., Zhang, Z., Pu, Z. and Wang, F.: Numerical simulations of an advection fog event over Shanghai
1024 Pudong International Airport with the WRF model, *J. Meteorol. Res.*, 31(5), 874–889,
1025 <https://doi.org/10.1007/s13351-017-6187-2>, 2017.
- 1026 Mahto, S. S. and Mishra, V.: Does ERA-5 outperform other reanalysis products for hydrologic applications
1027 in India?, *J. Geophys. Res. Atmos.*, <https://doi.org/10.1029/2019JD031155>, 2019.
- 1028 Masson, O., de Vismes Ott, A., Bourcier, L., Paulat, P., Ribeiro, M., Pichon, J.-M., Sellegri, K. and
1029 Gurriaran, R.: Change of radioactive cesium (137 Cs and 134 Cs) content in cloud water at an elevated
1030 site in France, before and after the Fukushima nuclear accident: Comparison with radioactivity in rainwater
1031 and in aerosol particles, *Atmos. Res.*, 151, 45–51, <https://doi.org/10.1016/j.atmosres.2014.03.031>, 2015.
- 1032 Mazoyer, M., Burnet, F., Denjean, C., Roberts, G. C., Haeffelin, M., Dupont, J.-C. and Elias, T.:
1033 Experimental study of the aerosol impact on fog microphysics, *Atmospheric Chemistry and Physics*, 19(7),
1034 4323–4344, <https://doi.org/10.5194/acp-19-4323-2019>, 2019.
- 1035 Mohan, T. S., Temimi, M., Ajayamohan, R. S., Nelli, N. R., Fonseca, R., Weston, M. and Valappil, V.: On
1036 the Investigation of the Typology of Fog Events in an Arid Environment and the Link with Climate Patterns,



- 1037 Mon. Wea. Rev., 148(8), 3181–3202, <https://doi.org/10.1175/MWR-D-20-0073.1>, 2020.
- 1038 Nakanishi, M. and Niino, H.: An Improved Mellor–Yamada Level-3 Model: Its Numerical Stability and
1039 Application to a Regional Prediction of Advection Fog, *Boundary Layer Meteorol.*, 119(2), 397–407,
1040 <https://doi.org/10.1007/s10546-005-9030-8>, 2006.
- 1041 Nelli, N. R., Temimi, M., Fonseca, R. M., Weston, M. J., Thota, M. S., Valappil, V. K., Branch, O.,
1042 Wulfmeyer, V., Wehbe, Y., Al Hosary, T., Shalaby, A., Al Shamsi, N. and Al Naqbi, H.: Impact of
1043 roughness length on WRF simulated land-atmosphere interactions over a hyper-arid region, *Earth and
1044 Space Science*, 7(6), <https://doi.org/10.1029/2020EA001165>, 2020a.
- 1045 Nelli, N., Fissehaye, S., Francis, D., Fonseca, R., Temimi, M., Weston, M., Abida, R. and Nesterov, O.:
1046 Characteristics of atmospheric aerosols over the UAE inferred from CALIPSO and Sun Photometer Aerosol
1047 Optical Depth, *Earth and Space Science Open Archive*, <https://doi.org/10.1002/essoar.10504057.1>, 2020b.
- 1048 Nelli, N., Francis, D., Fonseca, R., Bosc, E., Addad, Y., Temimi, M., Abida, R., Weston, M. and Cherif,
1049 C.: Characterization of the atmospheric circulation near the Empty Quarter Desert during major weather
1050 events, *Front. Environ. Sci.*, 10, <https://doi.org/10.3389/fenvs.2022.972380>, 2022.
- 1051 Nelli, N. R., Temimi, M., Fonseca, R., Francis, D., Nesterov, O., Abida, R., Weston, M. and Kumar, A.:
1052 Anatomy of the annular solar eclipse of 26 december 2019 and its impact on land– atmosphere interactions
1053 over an arid region, *IEEE Geosci. Remote Sensing Lett.*, 18(8), 1312–1316,
1054 <https://doi.org/10.1109/LGRS.2020.3003084>, 2021a.
- 1055 Nelli, N. R., Francis, D., Fonseca, R., Abida, R., Weston, M., Wehbe, Y. and Al Hosary, T.: The
1056 atmospheric controls of extreme convective events over the southern Arabian Peninsula during the spring
1057 season, *Atmos. Res.*, 262, 105788, <https://doi.org/10.1016/j.atmosres.2021.105788>, 2021b.
- 1058 Nesterov, O., Temimi, M., Fonseca, R., Nelli, N. R., Addad, Y., Bosc, E. and Abida, R.: Validation and
1059 statistical analysis of the Group for High Resolution Sea Surface Temperature data in the Arabian Gulf,
1060 *Oceanologia*, 63(4), 497–515, <https://doi.org/10.1016/j.oceano.2021.07.001>, 2021.
- 1061 Niu, S., Lu, C., Liu, Y., Zhao, L., Lü, J. and Yang, J.: Analysis of the microphysical structure of heavy fog
1062 using a droplet spectrometer: A case study, *Adv. Atmos. Sci.*, 27(6), 1259–1275,
1063 <https://doi.org/10.1007/s00376-010-8192-6>, 2010.
- 1064 Pérez-Díaz, J., Ivanov, O., Peshev, Z., Álvarez-Valenzuela, M., Valiente-Blanco, I., Evgenieva, T.,
1065 Dreischuh, T., Gueorguiev, O., Todorov, P. and Vaseashta, A.: Fogs: physical basis, characteristic
1066 properties, and impacts on the environment and human health, *Water (Basel)*, 9(10), 807,
1067 <https://doi.org/10.3390/w9100807>, 2017.
- 1068 Pleim, J. E.: A combined local and nonlocal closure model for the atmospheric boundary layer. part I: model
1069 description and testing, *J. Appl. Meteor. Climatol.*, 46(9), 1383–1395, <https://doi.org/10.1175/JAM2539.1>,
1070 2007.
- 1071 Rao, K. G. and Narendra Reddy, N.: Surface layer structure for ten categories of land surfaces of the Indian
1072 region with instrumented Mini Boundary Layer Mast Network (MBLM-Net) establishment during
1073 PRWONAM, *Journal of Atmospheric and Solar-Terrestrial Physics*, 173, 66–95,
1074 <https://doi.org/10.1016/j.jastp.2018.03.014>, 2018.
- 1075 Rao, K. G. and Reddy, N. N.: On moisture flux of the indian summer monsoon: A new perspective,
1076 *Geophys. Res. Lett.*, 46(3), 1794–1804, <https://doi.org/10.1029/2018GL080392>, 2019.
- 1077 Rao, K. G., Narendra Reddy, N., Ramakrishna, G., Bhuyan, P. K., Bhuyan, K., Kalita, G. and Pathak, B.:
1078 Near surface atmospheric response to the Total Solar Eclipse at Dibrugarh on 22 July 2009, *Journal of
1079 Atmospheric and Solar-Terrestrial Physics*, 95–96, 87–95, <https://doi.org/10.1016/j.jastp.2013.01.001>,



- 1080 2013.
- 1081 Reddy, N. N. and Rao, K. G.: Contrasting variations in the surface layer structure between the convective
1082 and non-convective periods in the summer monsoon season for Bangalore location during PRWONAM,
1083 Journal of Atmospheric and Solar-Terrestrial Physics, 167, 156–168,
1084 <https://doi.org/10.1016/j.jastp.2017.11.017>, 2018.
- 1085 Rose, T., Crewell, S., Löhnert, U. and Simmer, C.: A network suitable microwave radiometer for
1086 operational monitoring of the cloudy atmosphere, Atmos. Res., 75(3), 183–200,
1087 <https://doi.org/10.1016/j.atmosres.2004.12.005>, 2005.
- 1088 Schmetz, J., Pili, P., Tjemkes, S., Just, D., Kerkmann, J., Rota, S. and Ratier, A.: Supplement to an
1089 introduction to meteosat second generation (MSG), Bull. Amer. Meteor. Soc., 83(7), 992–992,
1090 [https://doi.org/10.1175/1520-0477\(2002\)083<0992:STAITM>2.3.CO;2](https://doi.org/10.1175/1520-0477(2002)083<0992:STAITM>2.3.CO;2), 2002.
- 1091 Seinfeld, J. H., Pandis, S. N. and Noone, K.: *atmospheric chemistry and physics: from air pollution to*
1092 *climate change*, Phys. Today, 51(10), 88–90, <https://doi.org/10.1063/1.882420>, 1998.
- 1093 Skamarock, W., Klemp, J., Dudhia, J., Gill, D., Barker, D., Wang, W., Huang, X.-Y. and Duda, M.: A
1094 Description of the Advanced Research WRF Version 3, UCAR/NCAR, <https://doi.org/10.5065/d68s4mrv>,
1095 2008.
- 1096 Spirig, R., Vogt, R. and Feigenwinter, C.: Droplet size distribution, liquid water content and water input of
1097 the seasonally variable, nocturnal fog in the Central Namib Desert, Atmos. Res., 262, 105765,
1098 <https://doi.org/10.1016/j.atmosres.2021.105765>, 2021.
- 1099 Stohl, A., Forster, C., Frank, A., Seibert, P. and Wotawa, G.: Technical note: The Lagrangian particle
1100 dispersion model FLEXPART version 6.2, Atmospheric Chemistry and Physics, 5(9), 2461–2474,
1101 <https://doi.org/10.5194/acp-5-2461-2005>, 2005.
- 1102 Tahir, Z. ul R., Azhar, M., Mumtaz, M., Asim, M., Moeenuddin, G., Sharif, H. and Hassan, S.: Evaluation
1103 of the reanalysis surface solar radiation from NCEP, ECMWF, NASA, and JMA using surface observations
1104 for Balochistan, Pakistan, J. Renewable Sustainable Energy, 12(2), 023703,
1105 <https://doi.org/10.1063/1.5135381>, 2020.
- 1106 Taraphdar, S., Pauluis, O. M., Xue, L., Liu, C., Rasmussen, R., Ajayamohan, R. S., Tessendorf, S., Jing,
1107 X., Chen, S. and Grabowski, W. W.: WRF Gray-Zone Simulations of Precipitation Over the Middle-East
1108 and the UAE: Impacts of Physical Parameterizations and Resolution, Journal of Geophysical Research:
1109 Atmospheres, 126, e2021JD034648, 2021.
- 1110 Tav, J., Masson, O., Burnet, F., Paulat, P., Bourriane, T., Conil, S. and Pourcelot, L.: Determination of
1111 fog-droplet deposition velocity from a simple weighing method, Aerosol and Air Quality Research, 18,
1112 103–113, 2018.
- 1113 Temimi, M., Fonseca, R. M., Nelli, N. R., Valappil, V. K., Weston, M. J., Thota, M. S., Wehbe, Y. and
1114 Yousef, L.: On the analysis of ground-based microwave radiometer data during fog conditions, Atmos.
1115 Res., 231, 104652, <https://doi.org/10.1016/j.atmosres.2019.104652>, 2020a.
- 1116 Temimi, M., Fonseca, R., Nelli, N., Weston, M., Thota, M., Valappil, V., Branch, O., Wizemann, H.-D.,
1117 Kondapalli, N. K., Wehbe, Y., Al Hosary, T., Shalaby, A., Al Shamsi, N. and Al Naqbi, H.: Assessing the
1118 impact of changes in land surface conditions on WRF predictions in arid regions, J. Hydrometeor, 1–60,
1119 <https://doi.org/10.1175/JHM-D-20-0083.1>, 2020b.
- 1120 Thalmann, E., Burkard, R., Wrzesinsky, T., Eugster, W. and Klemm, O.: Ion fluxes from fog and rain to an
1121 agricultural and a forest ecosystem in Europe, Atmos. Res., 64(1–4), 147–158,
1122 [https://doi.org/10.1016/S0169-8095\(02\)00087-X](https://doi.org/10.1016/S0169-8095(02)00087-X), 2002.



- 1123 Westbeld, A., Klemm, O., Griebbaum, F., Sträter, E., Larrain, H., Osses, P. and Cereceda, P.: Fog
1124 deposition to a *Tillandsia* carpet in the Atacama Desert, *Ann. Geophys.*, 27(9), 3571–3576,
1125 <https://doi.org/10.5194/angeo-27-3571-2009>, 2009.
- 1126 Weston, M. and Temimi, M.: Application of a nighttime fog detection method using SEVIRI over an arid
1127 environment, *Remote Sens (Basel)*, 12(14), 2281, <https://doi.org/10.3390/rs12142281>, 2020.
- 1128 Weston, M., Temimi, M., Burger, R. and Piketh, S.: A fog climatology at Abu Dhabi international airport,
1129 *J. Appl. Meteor. Climatol.*, 60(2), 223–236, <https://doi.org/10.1175/JAMC-D-20-0168.1>, 2021a.
- 1130 Weston, M., Francis, D., Nelli, N., Fonseca, R., Temimi, M. and Addad, Y.: The first characterization of
1131 fog microphysics in the united arab emirates, an arid region on the arabian peninsula, *Earth and Space
1132 Science*, 9(2), <https://doi.org/10.1029/2021EA002032>, 2022.
- 1133 Weston, M. J., Temimi, M., Nelli, N. R., Fonseca, R. M., Thota, M. S. and Valappil, V. K.: On the Analysis
1134 of the Low-Level Double Temperature Inversion Over the United Arab Emirates: A Case Study During
1135 April 2019, *IEEE Geosci. Remote Sensing Lett.*, 18(2), 346–350,
1136 <https://doi.org/10.1109/LGRS.2020.2972597>, 2021b.